Chapter one

Introduction

1.1.Introduction:

To make sense of any clinical problem, integrating the clinical information is essential. Specific features to be delineated in the clinical context include the child's age, sex, current and previous systemic illnesses, immunodeficiency states, medications, family history, along with a good clinical examination. Imaging has many roles: the first is to establish or substantiate the diagnosis and ascertain whether further (often more invasive) examinations are required; the second is to determine the extent of the disease, its natural history, and the effects of therapy. Pediatric interstitial lung disease is rare. The spectrum of diseases is different from that described in adults and is usually categorized into those with a known cause (e.g., aspiration syndromes and bronchopulmonary dysplasia) and those with an unknown cause (e.g., fibrosing lung disease and pulmonary hemosiderosis). A debate persists regarding which conditions should be included under the heading of pediatric interstitial lung disease, a term defined by Bokulic and Hilman (2005) as a heterogeneous group of disorders characterized by inflammation of the pulmonary interstitium. Because of the rarity of pediatric interstitial lung disease, there is a paucity of literature on the imaging of patients and few studies of thin section CT appearances. Fan and Langston (2004) stated that "our early experience in pediatric interstitial lung disease is similar to the adult experience in that high-resolution CT is generally more useful than a plain chest radiograph in defining severity and extent of disease." CT provides useful information regarding an optimum site for open lung biopsy when no cause for interstitial lung disease is identified and, as in adults, when findings on chest

radiographs appear normal. Because of the greater radiation dose given during CT than during chest radiography, it is important to evaluate the diagnostic gain of the technique in such a susceptible population accuracy of thin-section CT in comparison with chest radiographs for the diagnosis of pediatric interstitial lung disease. A higher proportion of pediatric interstitial lung diseases can be diagnosed on thin-section er than on chest radiographs. The confident and correct diagnoses were made more frequently with CT than with chest radiographs. The natural contrast between the air and the respiratory airways, and the low radiation dose, makes the chest radiograph the first line technique for most patients despite recent advances in imaging. Younger children are usually examined supine and older cooperative children can be examined erect. The routine use of lateral chest radiographs is unnecessary in pediatrics, but this projection should be reserved for certain clinical situations. An expiration film, in selected cases, can be taken to show good compliance of the lungs, suggesting that no over-inflation or air trapping is present. The radiologist's armamentarium includes the plain chest radiograph, ultrasound, fluoroscopy, computed tomography, magnetic resonance imaging, and nuclear medicine scintigraphy. When the chest radiograph is non-specific, high resolution computed tomography (HRCT) has been shown in adultsl-3 and in children4 to be more sensitive (it can detect abnormalities when the chest radiograph is normal); it also shows greater accuracy in characterizing diseases. HRCT usually involves sampling 1 mm sections of lung at 10-15 mm intervals, and examining on a high spatial resolution algorithm with a wide window width. HRCT is the imaging modality of choice for the morphological assessment of pulmonary parenchyma with excellent spatial resolution. The trade-off in increased sensitivity and specificity of HRCT over chest radiography is related to radiation dose (which is higher); however, conventional spiral or volumetric computed tomography (CT) has an even higher radiation burden than

HRCT. The use of low dose (50 mA, 0.75 s) limited CT mm slices every 10-20 mm) HRCT in inspiration with three expiratory supplementary scans allows accurate assessment of the presence and extent of diffuse lung disease at a dose equivalent to approximately 10--15 chest radiograph. This compares to a dose for volumetric chest CT (which acquires a whole spiral volume of lung) of approximately 50 chest radiographs if low dose pediatric protocols arc adhered to. If a child is unable to breath hold, the scans can be performed during quiet breathing and decubitus scans replace expiratory scans (the dependent lung behaving as the "expiratory lung" and the non-dependent lung as the "inspiratory lung"). The clinical indications for HRCT} in children are delineation of lung anatomy, study of both interstitial and airways disease, and dynamic studies to assess air trapping when expiratory/decubitus images are used. Advances in volumetric or spiral CT technology, particularly the development of multislice scanners, have resulted in faster scan acquisition times, and this, combined with reduction in the tube current, can allow the radiation dose to be kept to a minimum.

1.1. Chest Anatomy

The thorax (or chest) is the region of the body between the neck and the abdomen. It is flattened in front and behind but rounded at the sides. The framework of the walls of the thorax, which is referred to as the thoracic cage, is formed by the vertebral column behind, the ribs and intercostal spaces on either side, and the sternum and costal cartilages in front. Superiorly the thorax communicates with the neck, and inferiorly it is separated from the abdomen by the diaphragm. The thoracic cage protects the lungs and heart and affords attachment for the muscles of the thorax, upper extremity, abdomen, and back. The cavity of the thorax can be divided into a median partition, called the mediastinum, and the laterally placed pleurae and lungs. The lungs are covered by

a thin membrane called the visceral pleura, which passes from each lung at its root (i.e., where the main air passages and blood vessels enter) to the inner surface of the chest wall, where it is called the parietal pleura. In this manner, two membranous sacs called the pleural cavities are formed, one on each side of the thorax, between the lungs and the thoracic walls.

1.1.1. Structure of the Thoracic Wall:

The thoracic wall is covered on the outside by skin and by muscles attaching the shoulder girdle to the trunk. It is lined with parietal pleura. The thoracic wall is formed posteriorly by the thoracic part of the vertebral column; anteriorly by the sternum and costal cartilages (Figure 1-1); laterally by the ribs and intercostal spaces; superiorly by the suprapleural membrane; and inferiorly by the diaphragm, which separates the thoracic cavity from the abdominal cavity.

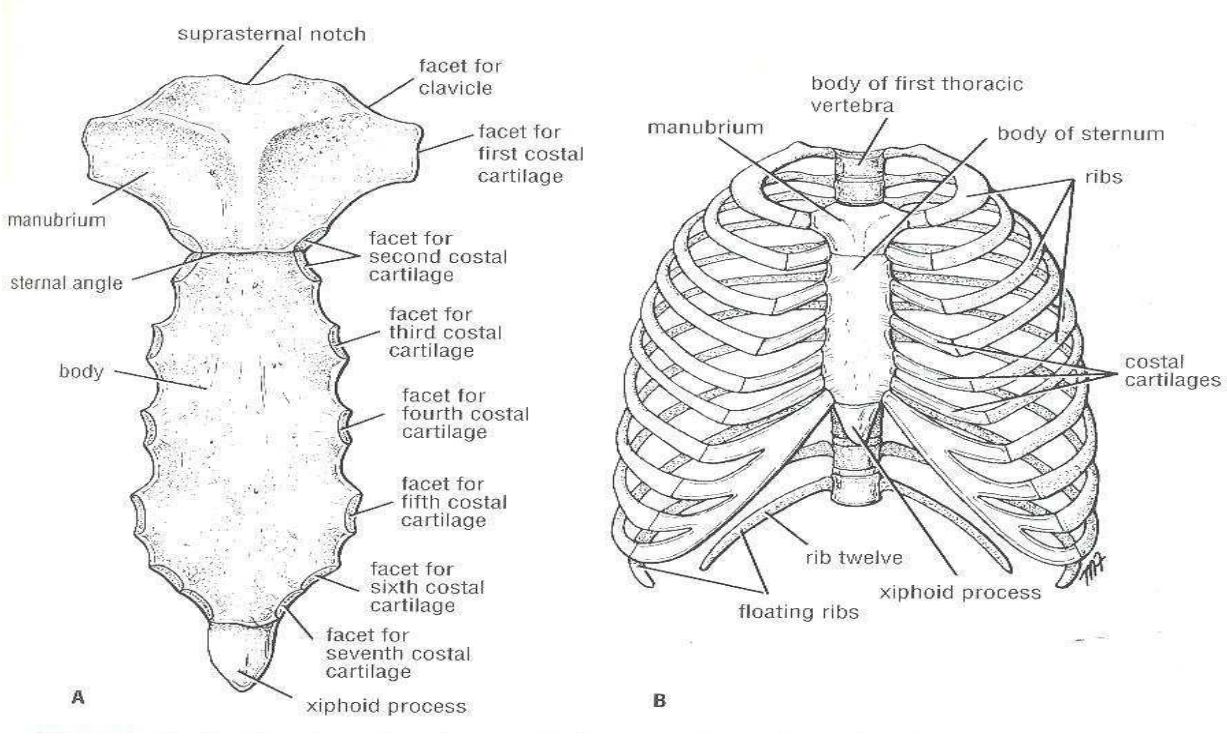

Figure 1.1. A: Anterior view of the Sternum B: Sternum, ribs and costal cartilage forming the thoracic skeleton

The sternum lies in the midline of the anterior chest wall. It is a flat bone that can be divided into three parts: manubrium sterni, body of the sternum, and xiphoid process. The manubrium is the upper part of the sternum. It articulates with the body of the sternum at the manubriosternal joint, and it also articulates with the clavicles and with the first costal cartilage and the upper part of the second costal cartilages on each side (Figure 1-1). It lies opposite the third and fourth thoracic vertebrae. The body of the sternum articulates above with the manubrium at the manubriosternal joint and below with the xiphoid process at the xiphisternal joint. On each side it articulates with the second to the seventh costal cartilages (Figure 1-1). The xiphoid process (Figure 1-1) is a thin plate of cartilage that becomes ossified at its proximal end during adult life. No ribs or costal cartilages are attached to it. The sternal angle (angle of Louis), formed by the articulation of the manubrium with the body of the sternum, can be recognized by the presence of a transverse ridge on the anterior aspect of the sternum (Figure 1-2). The transverse ridge lies at the level of the second costal cartilage, the point from which all costal cartilages and ribs are counted. The sternal angle lies opposite the intervertebral disc between the fourth and fifth thoracic vertebrae. The xiphisternal joint lies opposite the body of the ninth thoracic vertebra (Figure 1-2).

There are 12 pairs of ribs, all of which are attached posteriorly to the thoracic vertebrae (Figures 1-1, 1-3, 1-4, and 1-5). The ribs are divided into three categories. Firstly; True ribs which are the upper seven pairs are attached anteriorly to the sternum by their costal cartilages. Secondly; false ribs which are the 8th, 9th, and 10th pairs of ribs are attached anteriorly to each other and to the 7th rib by means of their costal cartilages and small synovial joints. Thirdly; floating ribs which are the 11th and 12th pairs have no anterior attachment.

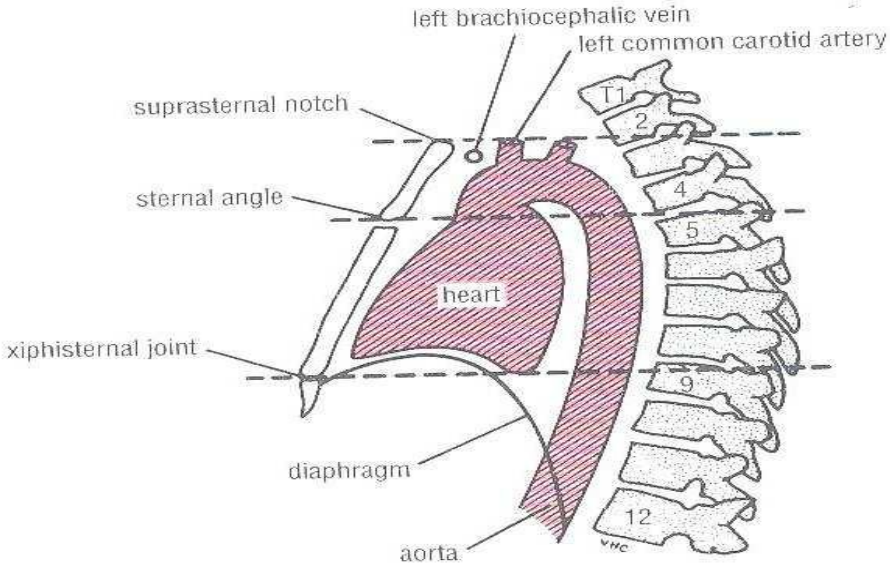

Figure 1-2. Lateral view of the thorax showing the relationship of the surface to vertebrae levels

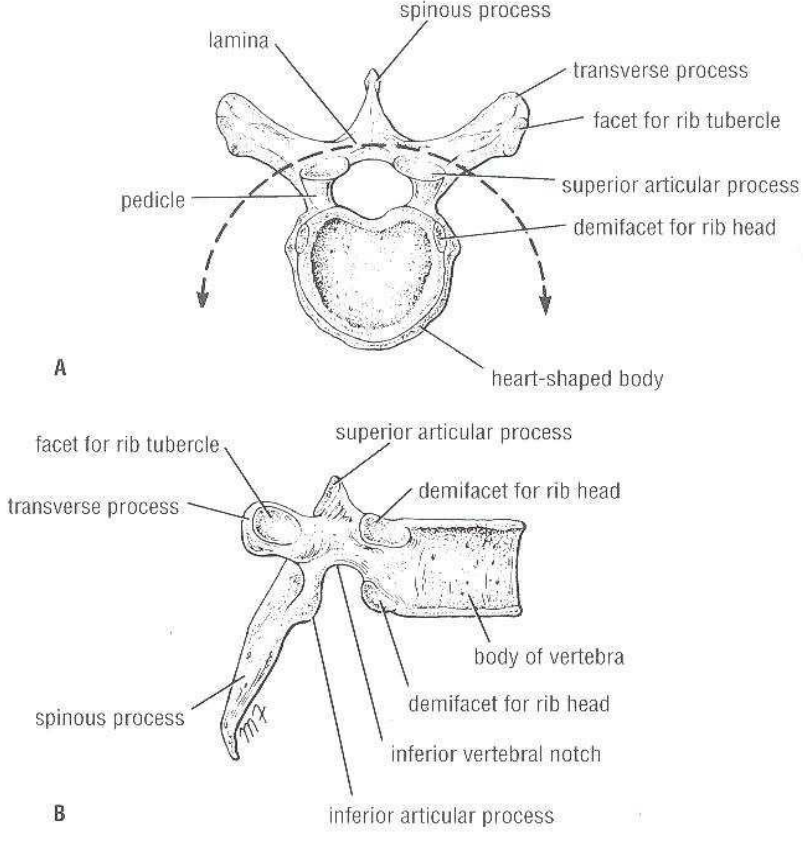

Figure 1-3. Thoracic vertebrae. A. Superior surface. B. Lateral surface

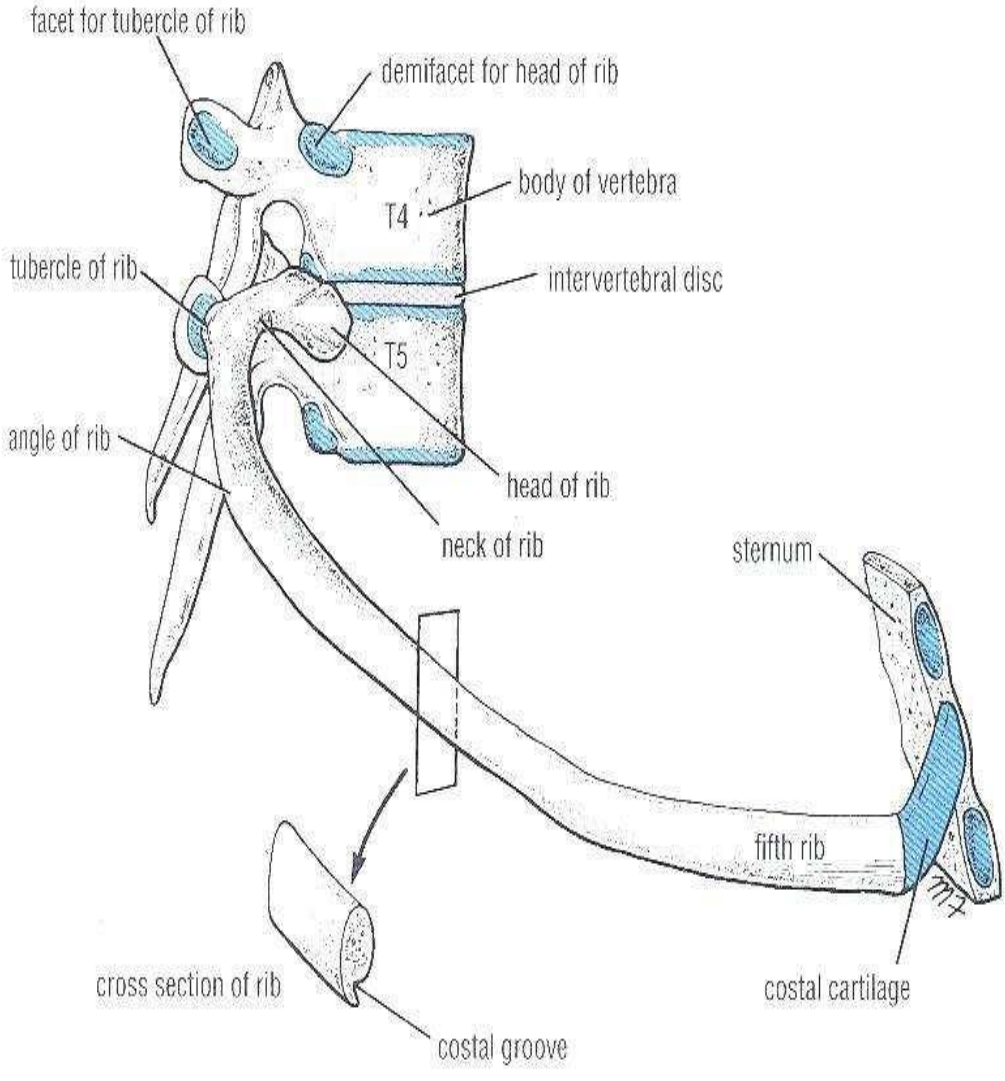

Figure 1-4. Fifth right ribs as it articulates with vertebral column posteriorly and the sternum anteriorly.

A typical rib is a long, twisted, flat bone having a rounded, smooth superior border and a sharp, thin inferior border (Figures 1-4 and Figure 1-5). The inferior border overhangs and forms the costal groove, which accommodates the intercostal vessels and nerve. The anterior end of each rib is attached to the corresponding costal cartilage (Figure 1-4).

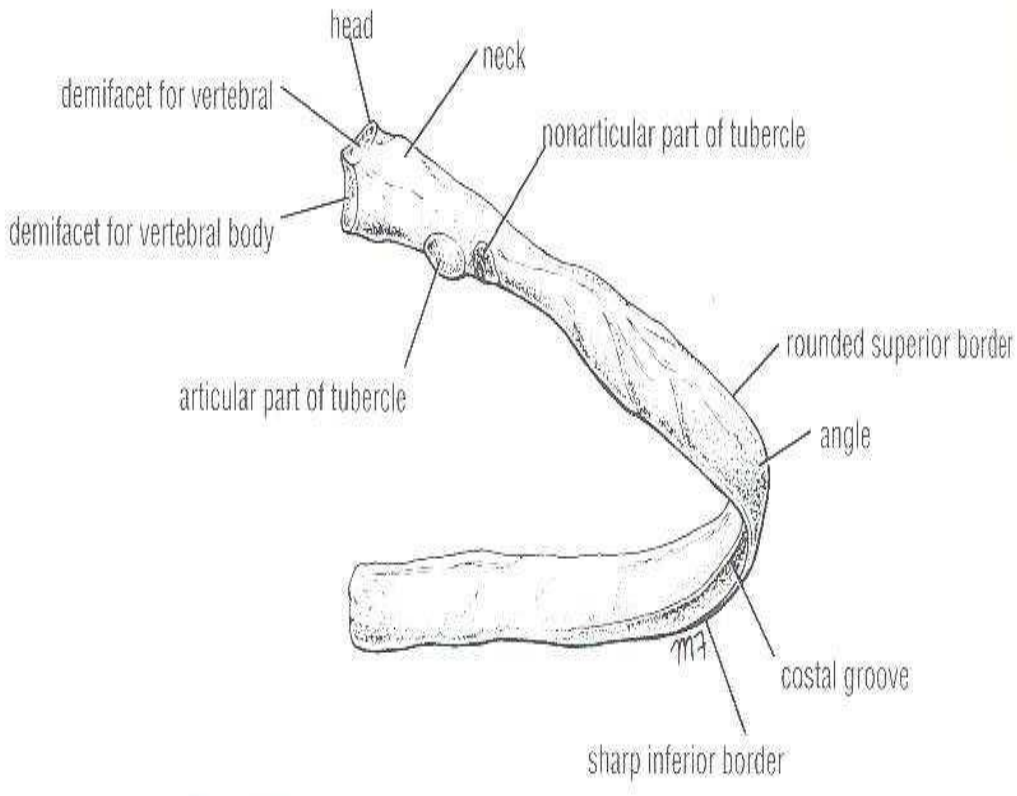

Figure 1-5. Fifth right rib, as seen from the posterior aspect.

A rib has a head, neck; tubercle, shaft, and angle (Figure 1-4 and Figure 1-5). The head has two facets for articulation with the numerically corresponding vertebral body and that of the vertebra immediately above (Figure 1-4). The neck is a constricted portion situated between the head and the tubercle. The tubercle is a prominence on the outer surface of the rib at the junction of the neck with the shaft. It has a facet for articulation with the transverse process of the numerically corresponding vertebra (Figure 1-4). The shaft is thin and flattened and twisted on its long axis. Its inferior border has the costal groove. The angle is where the shaft of the rib bends sharply forward.

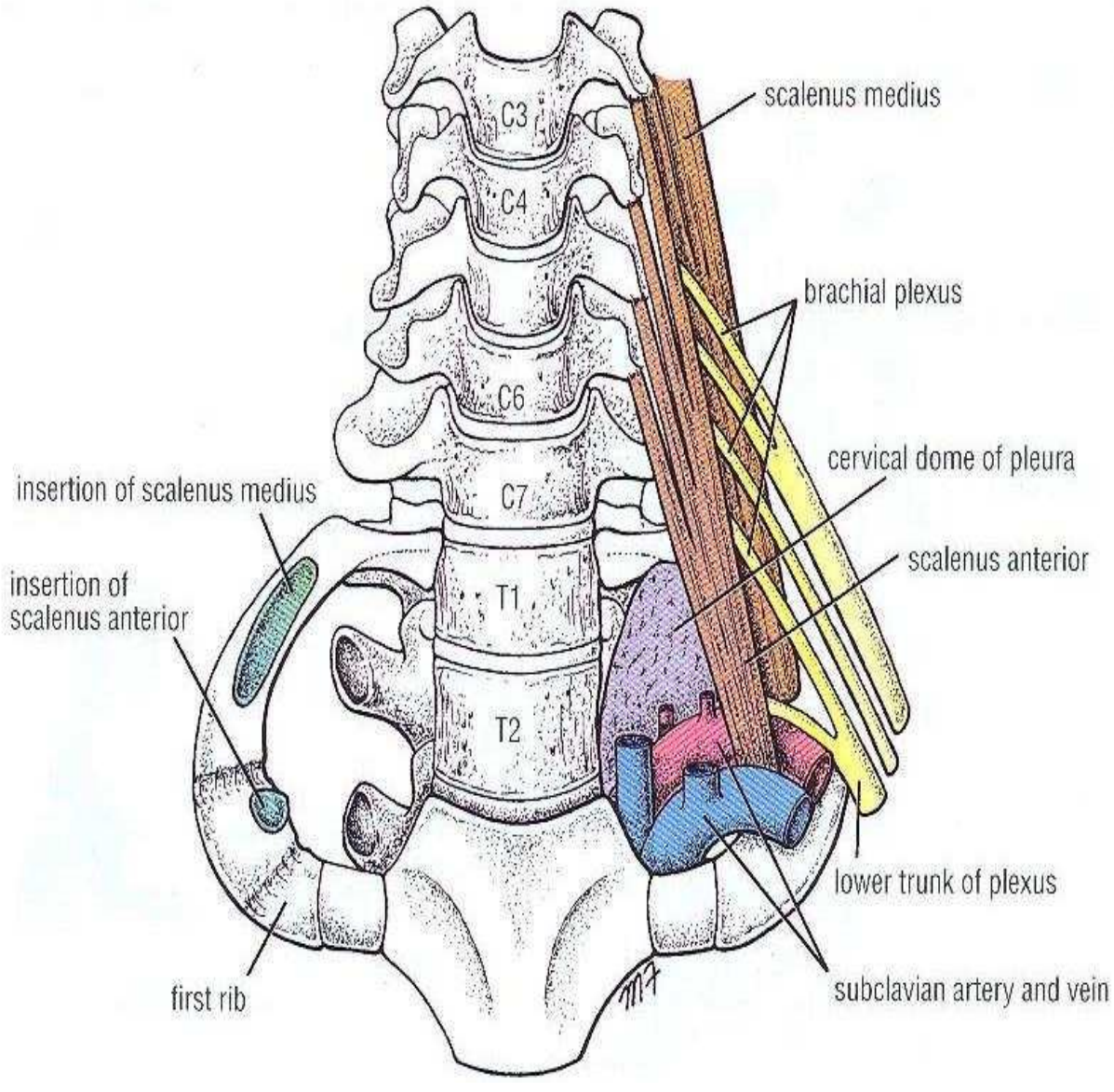

Figure 1-6. Thoracic outlet showing the cervical dome of pleura on the left side of the body and its relationship to inner borer of the first rib.

The first rib is important clinically because of its close relationship to the lower nerves of the brachial plexus and the main vessels to the arm, namely, the subclavian artery and vein (Figure 1-6). This rib is small and flattened from above downward. The scalenus anterior muscle is attached to its upper surface and inner border. Anterior to the scalenus anterior, the subclavian vein crosses the rib; posterior to the muscle attachment, the subclavian artery and the lower trunk of the brachial plexus cross the rib and lie in contact with the bone. Costal cartilages are bars of cartilage connecting the upper seven ribs to the lateral edge of the

sternum and the 8th, 9th, and 10th ribs to the cartilage immediately above. The cartilages of the 11th and 12th ribs end in the abdominal musculature (Figure 1-1).

The costal cartilages contribute significantly to the elasticity and mobility of the thoracic walls. In old age, the costal cartilages tend to lose some of their flexibility as the result of superficial calcification. The manubriosternal joint is a cartilaginous joint between the manubrium and the body of the sternum. A small amount of angular movement is possible during respiration. The xiphisternal joint is a cartilaginous joint between the xiphoid process (cartilage) and the body of the sternum. The xiphoid process usually fuses with the body of the sternum during middle age. The first rib and the three lowest ribs have a single synovial joint with their corresponding vertebral body. For the second to the ninth ribs, the head articulates by means of a synovial joint with the corresponding vertebral body and that of the vertebra above it (Figure 1-4). There is a strong intraarticular ligament that connects the head to the intervertebral disc. The tubercle of a rib articulates by means of a synovial joint with the transverse process of the corresponding vertebra (Fig. 2-4). (This joint is absent on the 11th and 12th ribs.) These joints are cartilaginous joints. No movement is possible.

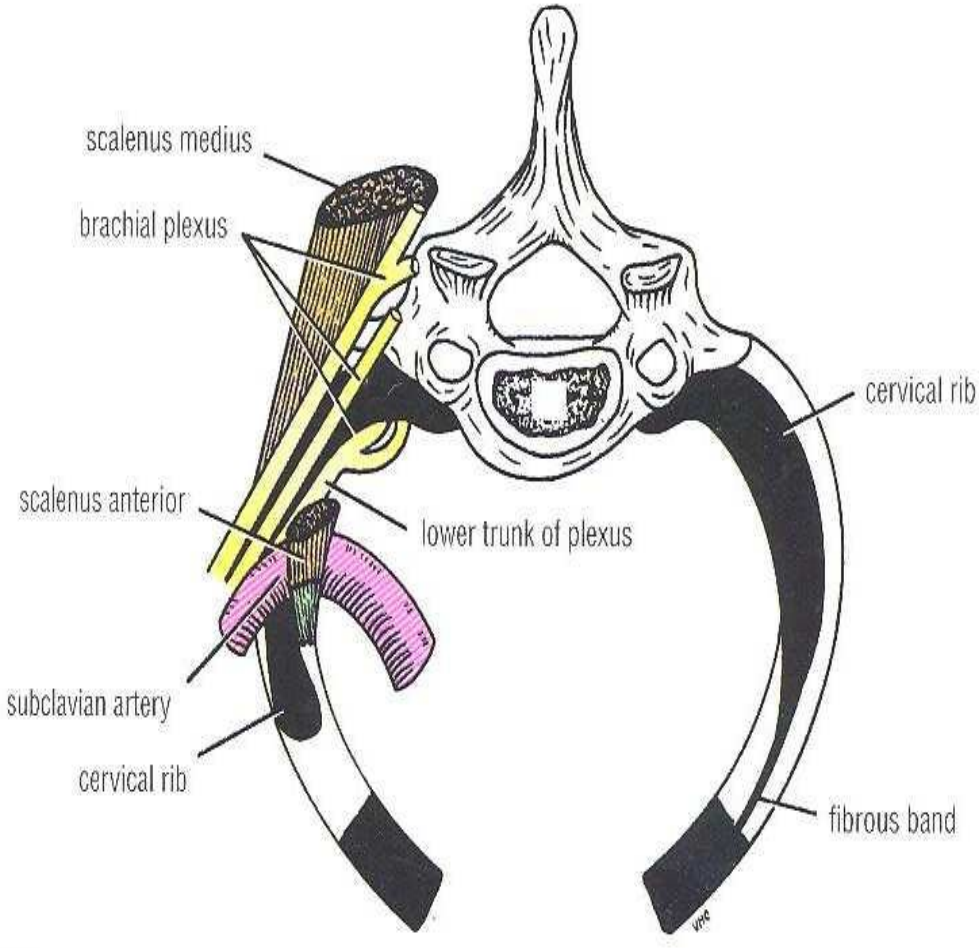

Figure 1-7. Thoracic outlet as seen from above.

The first costal cartilages articulate with the manubrium, by cartilaginous joints that permit no movement (Figure 1-1). The 2nd to the 7th costal cartilages articulate with the lateral border of the sternum by synovial joints. In addition, the 6th, 7th, 8th, 9th, and 10th costal cartilages articulate with one another along their borders by small synovial joints. The cartilages of the 11th and 12th ribs are embedded in the abdominal musculature. The 1st ribs and their costal cartilages are fixed to the manubrium and are immobile. The raising and lowering of the ribs during respiration are accompanied by movements in both the joints of the head and the tubercle, permitting the neck of each rib to rotate around its own axis.

The chest cavity communicates with the root of the neck through an opening called the thoracic outlet. It is called an outlet because important vessels and nerves emerge from the thorax here to enter the neck and upper limbs. The opening is bounded posteriorly by the first thoracic vertebra, laterally by the medial borders of the first ribs and their costal cartilages, and anteriorly by the superior border of the manubrium sterni. The opening is obliquely placed facing upward and forward. Through this small opening pass the esophagus and trachea and many vessels and nerves. Because of the obliquity of the opening, the apices of the lung and pleurae project upward into the neck. The thoracic cavity communicates with the abdomen through a large opening. The opening is bounded posteriorly by the 12th thoracic vertebra, laterally by the curving costal margin, and anteriorly by the xiphisternal joint. Through this large opening, which is closed by the diaphragm, pass the esophagus and many large vessels and nerves, all of which pierce the diaphragm. The spaces between the ribs contain three muscles of respiration: the external intercostal, the internal intercostal, and the innermost intercostal muscle. The innermost intercostal muscle is lined internally by the endothoracic fascia, which is lined internally by the parietal pleura. The intercostal nerves and blood vessels run between the intermediate and deepest layers of muscles (Figure 1-8). They are arranged in the following order from above downward: intercostal vein, intercostal artery, and intercostal nerve (i.e., VAN). The external intercostal muscle forms the most superficial layer. Its fibers are directed downward and forward from the inferior border of the rib above to the superior border of the rib below (Fig. 2-8).

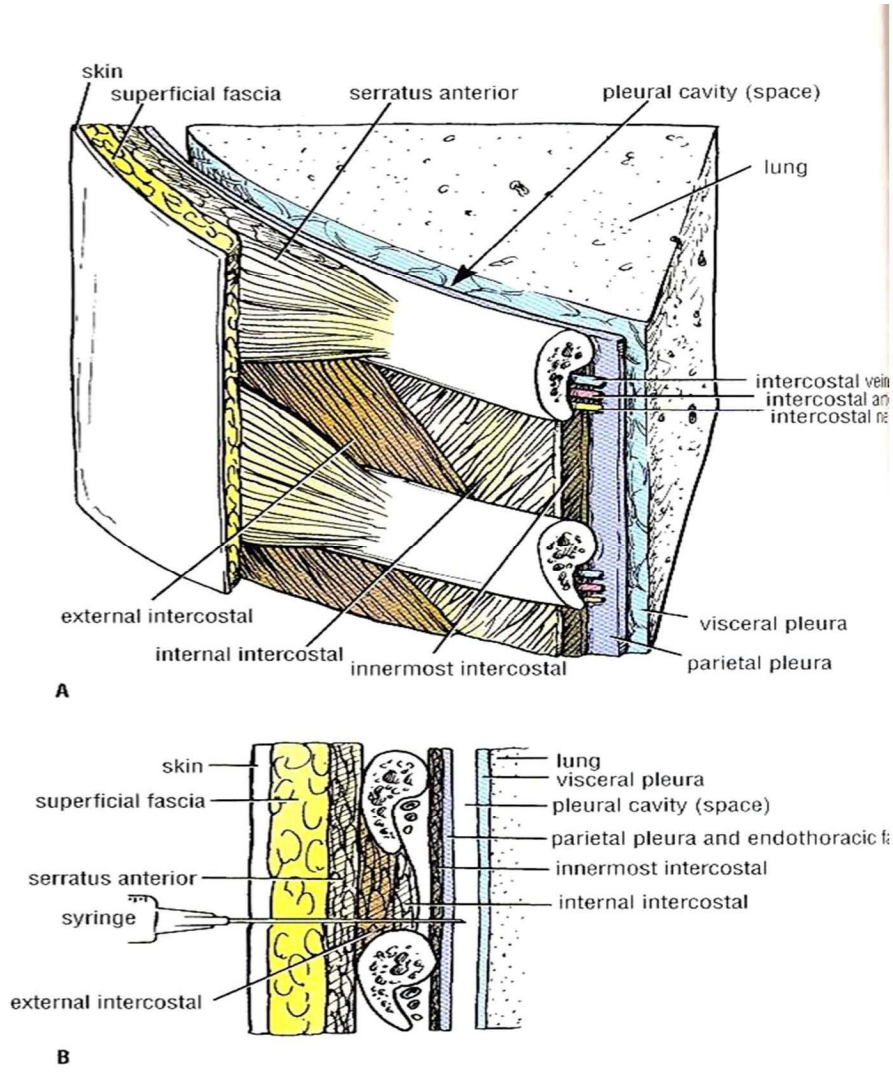

Figure 1-8. A. Section through an intercostal space, B. Structures penetrated by needle when it passes from skin surface to pleural cavity. Depending on the site of penetration, the pectoral muscles will be pierced in addition to the serratus anterior muscle.

The muscle extends forward to the costal cartilage where it is replaced by an aponeurosis, the anterior (external) intercostal membrane (Fig. 2-9).

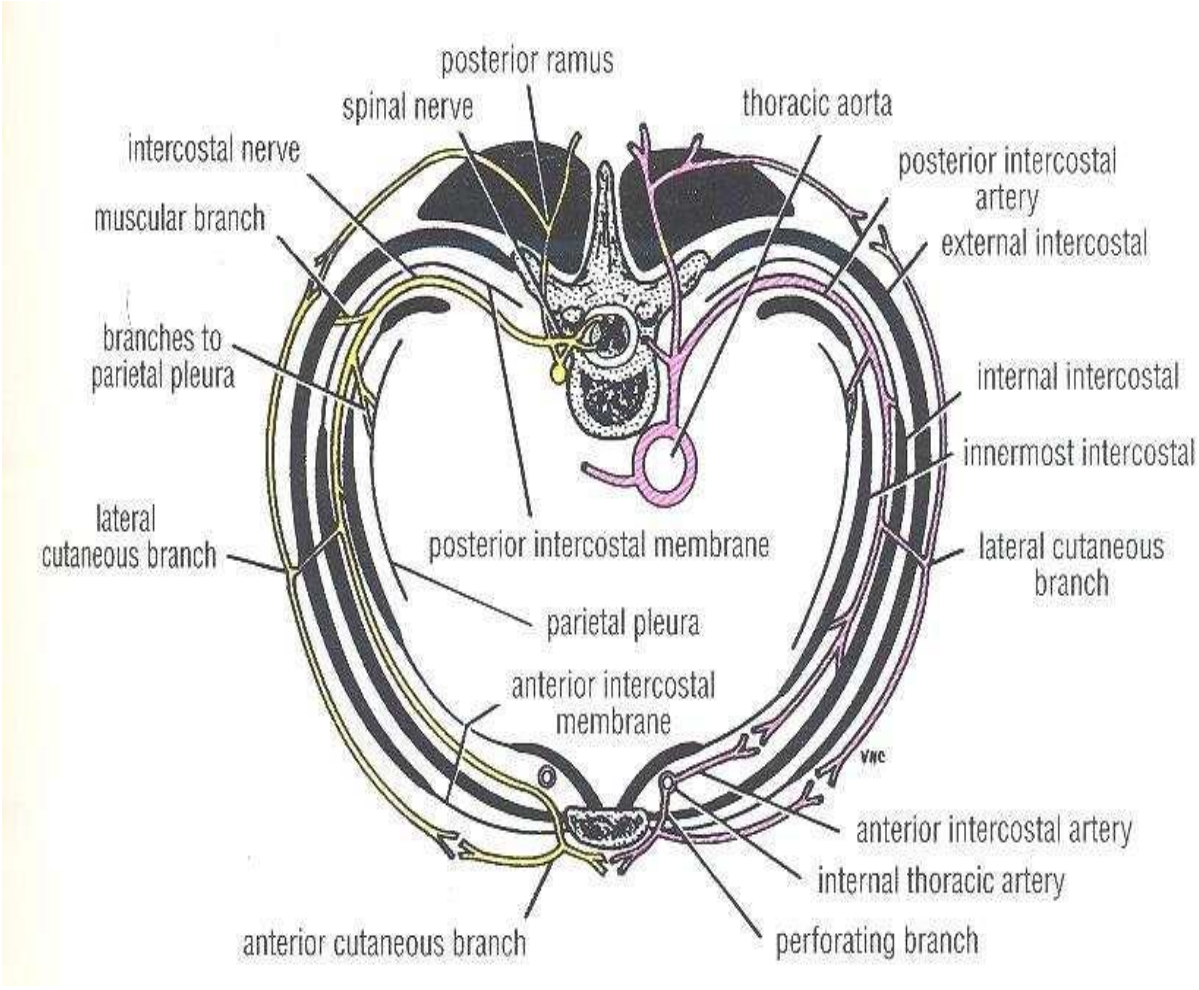

Figure 1-9. Cross section of the thorax showing distribution of a typical intercostal nerve and a posterior and an anterior intercostal artery.

The internal intercostal muscle forms the intermediate layer. Its fibers are directed downward and backward from the subcostal groove of the rib above to the upper border of the rib below (Figure 1-8). The muscle extends backward from the sternum in front to the angles of the ribs behind, where the muscle is replaced by an aponeurosis, the posterior (internal) intercostal membrane (Figure 1-9). The innermost intercostal muscle forms the deepest layer and corresponds to the transversus abdominis muscle in the anterior abdominal wall. It is an incomplete muscle layer and crosses more than one intercostal space within the ribs. It is related internally to fascia (endothoracic fascia) and parietal pleura and externally to the intercostal nerves and vessels. The innermost intercostal muscle can be

divided into three portions (Figure 1-9), which are more or less separate from one another action. When the intercostal muscles contract, they all tend to pull the ribs nearer to one another. If the 1st rib is fixed by the contraction of the muscles in the root of the neck, namely, the scalene muscles, the intercostal muscles raise the 2nd to the 12th ribs toward the first rib, as in inspiration. If, conversely, the 12th rib is fixed by the quadratus lumborum muscle and the oblique muscles of the abdomen, the 1st to the 11th ribs will be lowered by the contraction of the intercostal muscles, as in expiration. In addition, the tone of the intercostal muscles during the different phases of respiration serves to strengthen the tissues of the intercostal spaces, thus preventing the sucking in or the blowing out of the tissues with changes in intrathoracic pressure. For further details concerning the action of these muscles The intercostal muscles are supplied by the corresponding intercostal nerves. The intercostal nerves and blood vessels (the neurovascular bundle), as in the abdominal wall, run between the middle and innermost layers of muscles (Figure 1-8 and figure 1-9). They are arranged in the following order from above downward: intercostal vein, intercostal artery, and intercostal nerve (i.e., VAN). Each intercostal space contains a large single posterior intercostal artery and two small anterior intercostal arteries. The posterior intercostal arteries of the first two spaces are branches from the superior intercostal artery, a branch of the costocervical trunk of the subclavian artery. The posterior intercostal arteries of the lower nine spaces are branches of the descending thoracic aorta (Figure 1-9 and figure 1-10). The anterior intercostal arteries of the first six spaces are branches of the internal thoracic artery (Figure 1-9 and figure 1-10), which arises from the first part of the subclavian artery. The anterior intercostal arteries of the lower spaces are branches of the musculophrenic artery, one of the terminal branches of the internal thoracic artery. Each intercostal artery gives off branches to the muscles, skin, and parietal pleura. In the region of the breast in

the female, the branches to the superficial structures are particularly large. The corresponding posterior intercostal veins drain backward into the azygos or hemiazygos veins (Figure 1-10 and figure 1-11), and the anterior intercostal veins drain forward into the internal thoracic and musculophrenic veins.

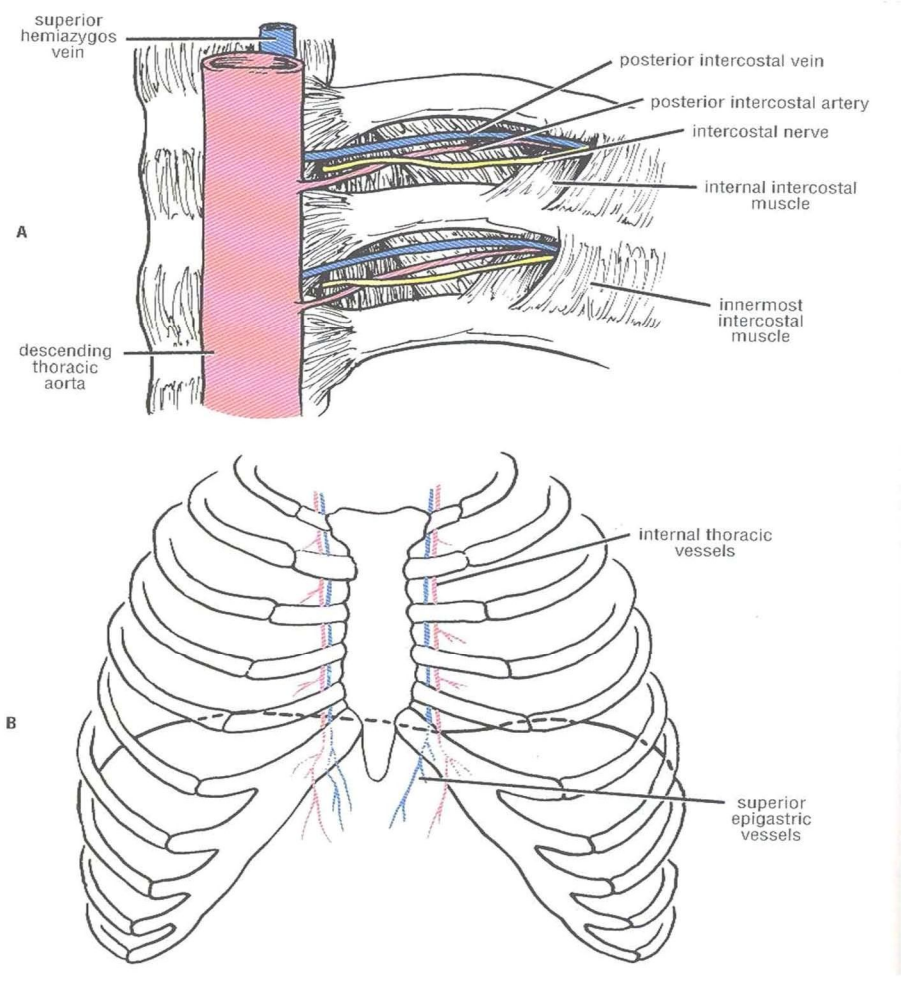

Figure 1-10. A. Internal view of the posterior end of two typical intercostal space; the posterior intercostal has been removed for clarity. B. Anterior view of the

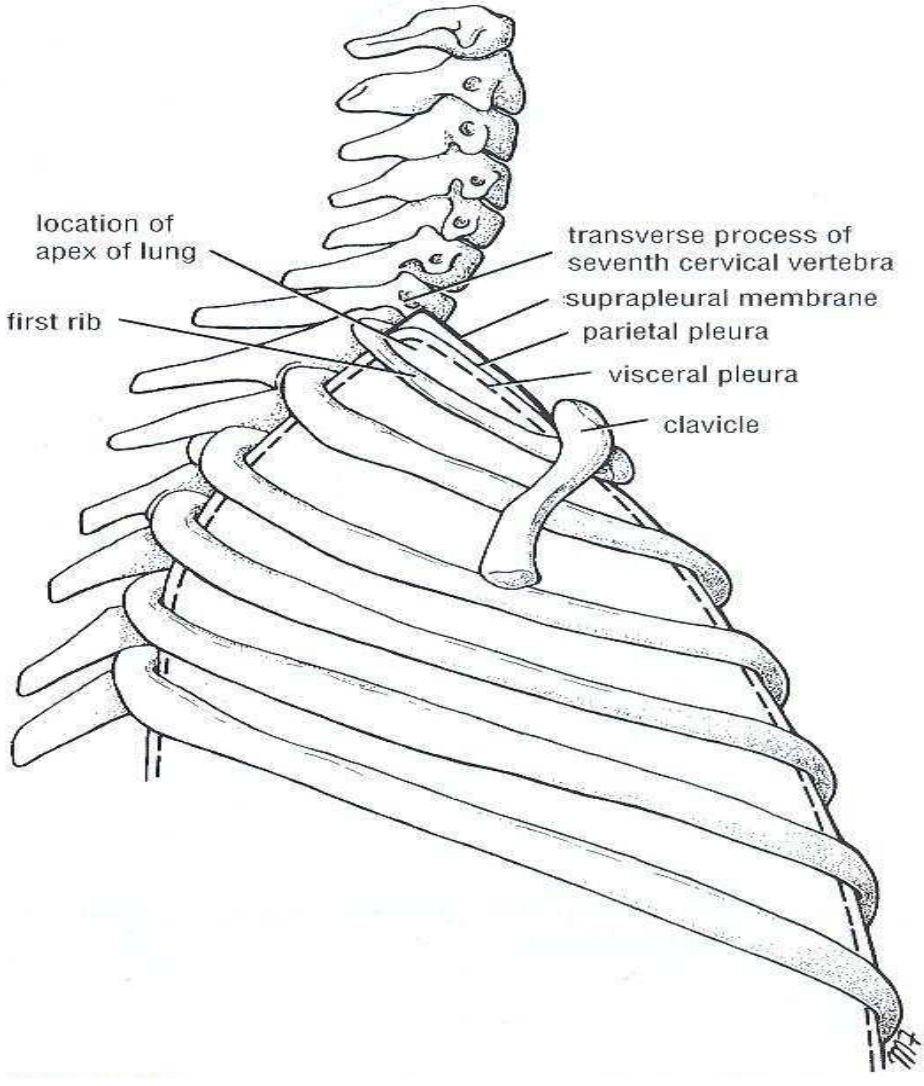

Figure 1-11. Lateral View of the upper opening of the Thoracic Cage showing how the apex of the lung projects superiorly into the root of the neck. The apex of the lung is covered with visceral and parietal layers of pleura and is protected by suprapleural membrane, which is a thickening of the endothoracic fascia.

The intercostal nerves are the anterior rami of the first 11 thoracic spinal nerves (Figure 2-12). The anterior ramus of the 12th thoracic nerve lies in the abdomen and runs forward in the abdominal wall as the subcostal nerve. Each intercostal nerve enters an intercostal space between the parietal pleura and the posterior intercostal membrane (Figure 1-8 and figure 1-9). It then runs forward inferiorly to the intercostal vessels in the subcostal groove of the corresponding rib,

between the innermost intercostal and internal intercostal muscle. The first six nerves are distributed within their intercostal spaces. The seventh to ninth intercostal nerves leave the anterior ends of their intercostal spaces by passing deep to the costal cartilages, to enter the anterior abdominal wall. The 10th and 11th nerves, since the corresponding ribs are floating, pass directly into the abdominal wall.

Rami communicants connect the intercostal nerve to a ganglion of the sympathetic trunk (Figure 1-26). The gray ramus joins the nerve medial at the point at which the white ramus leaves it. The collateral branch runs forward inferiorly to the main nerve on the upper border of the rib below. The lateral cutaneous branch reaches the skin on the side of the chest. It divides into an anterior and a posterior branch. The anterior cutaneous branch, which is the terminal portion of the main trunk, reaches the skin near the midline. It divides into a medial and a lateral branch. Muscular branches run to the intercostal muscles. Pleural sensory branches go to the parietal pleura. Peritoneal sensory branches (7th to 11th intercostal nerves only) run to the parietal peritoneum. The first intercostal nerve is joined to the brachial plexus by a large branch that is equivalent to the lateral cutaneous branch of typical intercostal nerves. The remainder of the first intercostal nerve is small, and there is no anterior cutaneous branch. The second intercostal nerve is joined to the medial cutaneous nerve of the arm by a branch called the intercostobrachial nerve, which is equivalent to the lateral cutaneous branch of other nerves. The second intercostal nerve therefore supplies the skin of the armpit and the upper medial side of the arm. In coronary artery disease, pain is referred along this nerve to the medial side of the arm. With the exceptions noted, the first six intercostal nerves therefore supply the skin and the parietal pleura covering the outer and inner surfaces of each intercostal space, respectively, and the intercostal muscles of each intercostal space and the

levatores costarum and serratus posterior muscles. In addition, the 7th to the 11th intercostal nerves supply the skin and the parietal peritoneum covering the outer and inner surfaces of the abdominal wall, respectively, and the anterior abdominal muscles, which include the external oblique, internal oblique, transversus abdominis, and rectus abdominis muscles. Superiorly, the thorax opens into the root of the neck by a narrow aperture, the thoracic outlet. The outlet transmits structures that pass between the thorax and the neck (esophagus, trachea, blood vessels, etc.) and for the most part lie close to the midline. On either side of these structures the outlet is closed by a dense facial layer called the suprapleural membrane (Figure 1-13). This tent-shaped fibrous sheet is attached laterally to the medial border of the first rib and costal cartilage. It is attached at its apex to the tip of the transverse process of the seventh cervical vertebra and medially to the fascia investing the structures passing from the thorax into the neck. It protects the underlying cervical pleura and resists the changes in intrathoracic pressure occurring during respiratory movements. The endothoracic fascia is a thin layer of loose connective tissue that separates the parietal pleura from the thoracic wall. The suprapleural membrane is a thickening of this fascia.

The diaphragm is a thin muscular and tendinous septum that separates the chest cavity above from the abdominal cavity below (Figure 1-16). It is pierced by the structures that pass between the chest and the abdomen. The diaphragm is the most important muscle of respiration. It is dome shaped and consists of a peripheral muscular part, which arises from the margins of the thoracic opening, and a centrally placed tendon (Figure 1-16). The origin of the diaphragm can be divided into three parts: A sternal part arising from the posterior surface of the xiphoid process (Figure 1-2) A costal part arising from the deep surfaces of the lower six ribs and their costal cartilages (Figure 1-16) A vertebral part arising by vertical columns or crura and from the accurate ligaments**.** The right crus arise

from the sides of the bodies of the first three lumbar vertebrae and the intervertebral discs; the left crus arise from the sides of the bodies of the first two lumbar vertebrae and the intervertebral disc (Figure 1-16). Lateral to the crura the diaphragm arises from the medial and lateral arcuate ligaments (Figure 1-16). The medial arcuate ligament extends from the side of the body of the second lumbar vertebra to the tip of the transverse process of the first lumbar vertebra. The lateral arcuate ligament extends from the tip of the transverse process of the first lumbar vertebra to the lower border of the 12th rib. The medial borders of the two crura are connected by a median arcuate ligament, which crosses over the anterior surface of the aorta (Figure 1-16).

The diaphragm is inserted into a central tendon, which is shaped like three leaves. The superior surface of the tendon is partially fused with the inferior surface of the fibrous pericardium. Some of the muscle fibers of the right crus pass up to the left and surround the esophageal orifice in a sling like loop. These fibers appear to act as a sphincter and possibly assist in the prevention of regurgitation of the stomach contents into the thoracic part of the esophagus (Figure 1-16). As seen from in front, the diaphragm curves up into right and left domes, or cupulae. The right dome reaches as high as the upper border of the fifth rib, and the left dome may reach the lower border of the fifth rib. (The right dome lies at a higher level, because of the large size of the right lobe of the liver.) The central tendon lies at the level of the xiphisternal joint. The domes support the right and left lungs, whereas the central tendon supports the heart. The levels of the diaphragm vary with the phase of respiration, the posture, and the degree of distention of the abdominal viscera. The diaphragm is lower when a person is sitting or standing; it is higher in the supine position and after a large meal. When seen from the side, the diaphragm has the appearance of an inverted J, the long limb extending up from the vertebral column and the short limb extending forward to the xiphoid

process (Figure 1-2). Motor nerve supply: The right and left phrenic nerves (C3, 4, 5) Sensory nerve supply: The parietal pleura and peritoneum covering the central surfaces of the diaphragm are from the phrenic nerve and the periphery of the diaphragm is from the lower six intercostal nerves.

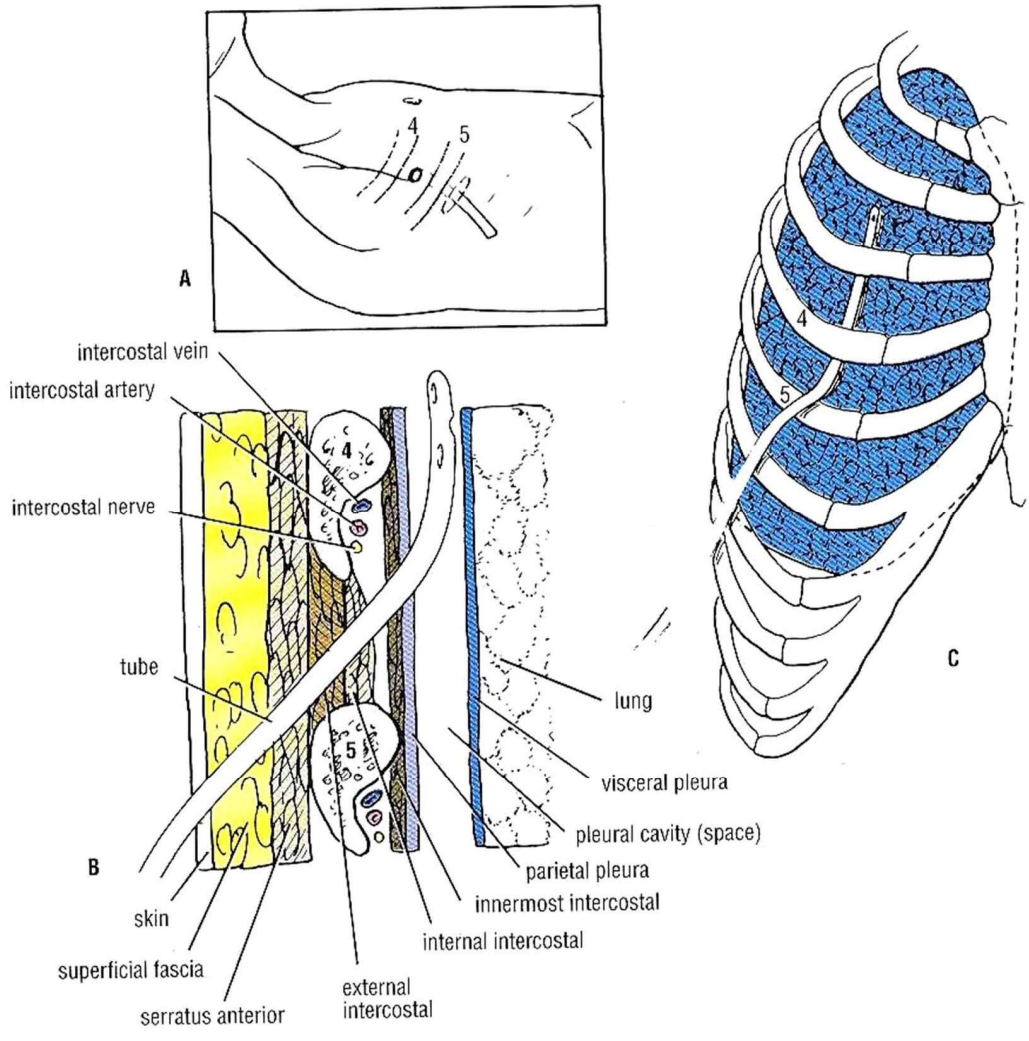

Figure 1-14. Tube thoracostomy. A. The site for insertion of the tube at anterior axillary line. B. the various layers of tissue penetrated by the scalpel and later the tube as they pass through the chest wall to enter the pleural cavity (space). C. the tube advancing superiorly and posteriorly in pleural space.

On contraction, the diaphragm pulls down its central tendon and increases the vertical diameter of the thorax. Muscle of inspiration: On contraction, the

diaphragm pulls its central tendon down and increases the vertical diameter of the thorax. The diaphragm is the most important muscle used in inspiration. Muscle of abdominal straining: The contraction of the diaphragm assists the contraction of the muscles of the anterior abdominal wall in raising the intra-abdominal pressure for micturition, defecation, and parturition. This mechanism is further aided by the person taking a deep breath and closing the glottis of the larynx. The diaphragm is unable to rise because of the air trapped in the respiratory tract. Now and again, air is allowed to escape, producing a grunting sound. Weight-lifting muscle: In a person taking a deep breath and holding it (fixing the diaphragm), the diaphragm assists the muscles of the anterior abdominal wall in raising the intra-abdominal pressure to such an extent that it helps support the vertebral column and prevent flexion. This greatly assists the postvertebral muscles in the lifting of heavy weights. Needless to say, it is important to have adequate sphincteric control of the bladder and anal canal under these circumstances. Thoracoabdominal pump: The descent of the diaphragm decreases the intrathoracic pressure and at the same time increases the intra-abdominal pressure. This pressure change compresses the blood in the inferior vena cava and forces it upward into the right atrium of the heart. Lymph within the abdominal lymph vessels is also compressed, and its passage upward within the thoracic duct is aided by the negative intrathoracic pressure. The presence of valves within the thoracic duct prevents backflow.

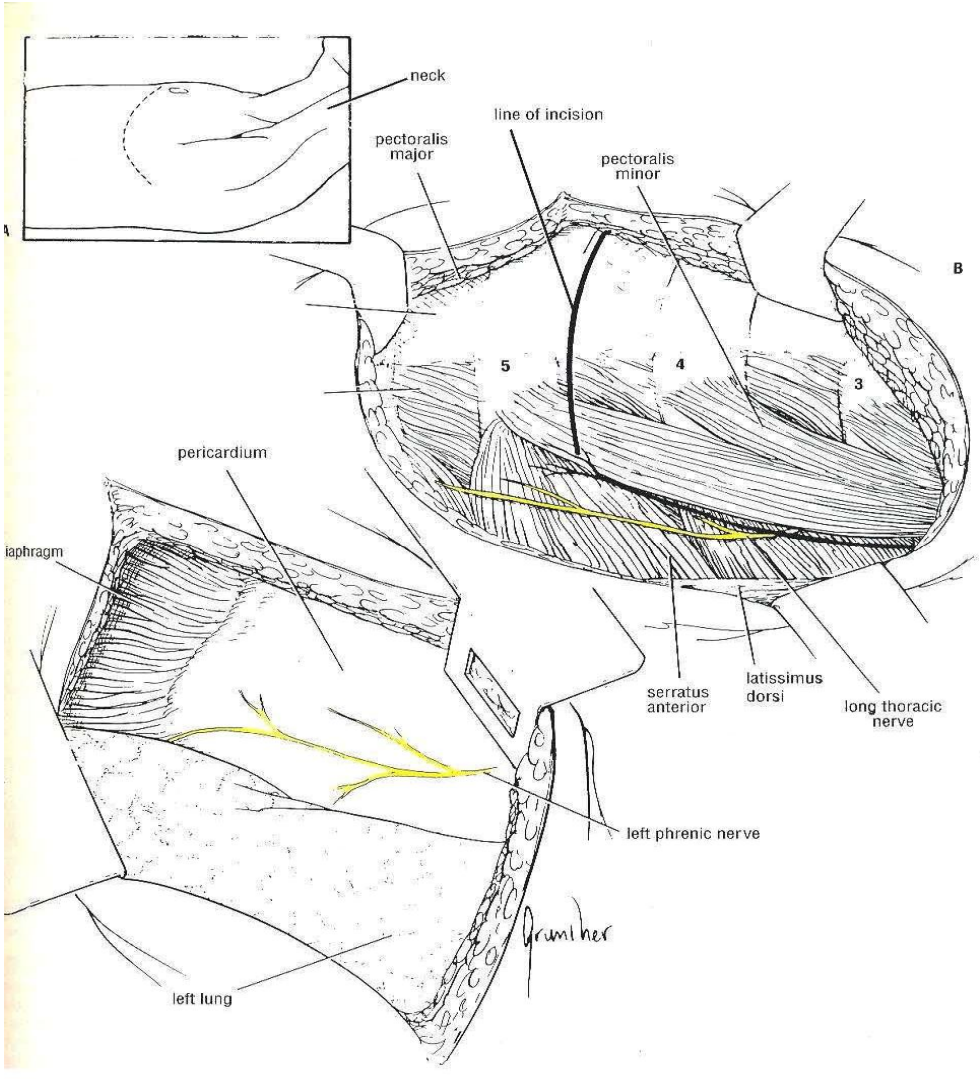

Figure 1-15. Left Thoracostomy. A. Site of skin incision over fourth intercostal space. B. the exposed ribs and associated muscles. C. the pleural space over the pericardium beneath the mediastinal pleura.

The aortic opening lies anterior to the body of the 12th thoracic vertebra between the crura (Figure 1-16). It transmits the aorta, the thoracic duct, and the azygos vein. The esophageal opening lies at the level of the 10th thoracic vertebra in a sling of muscle fibers derived from the right crus (Figure 1-16). It transmits the esophagus, the right and left vagus nerves, the esophageal branches of the left gastric vessels, and the lymphatics from the lower third of the esophagus. The

canal opening lies at the level of the eighth thoracic vertebra in the central tendon (Figure 1-16). It transmits the inferior vena cava and terminal branches of the right phrenic nerve. In addition to these openings, the sympathetic splanchnic nerves pierce the crura; the sympathetic trunks pass posterior to the medial arcuate ligament on each side; and the superior epigastric vessels pass between the sternal and costal origins of the diaphragm on each side (Figure 1-16).

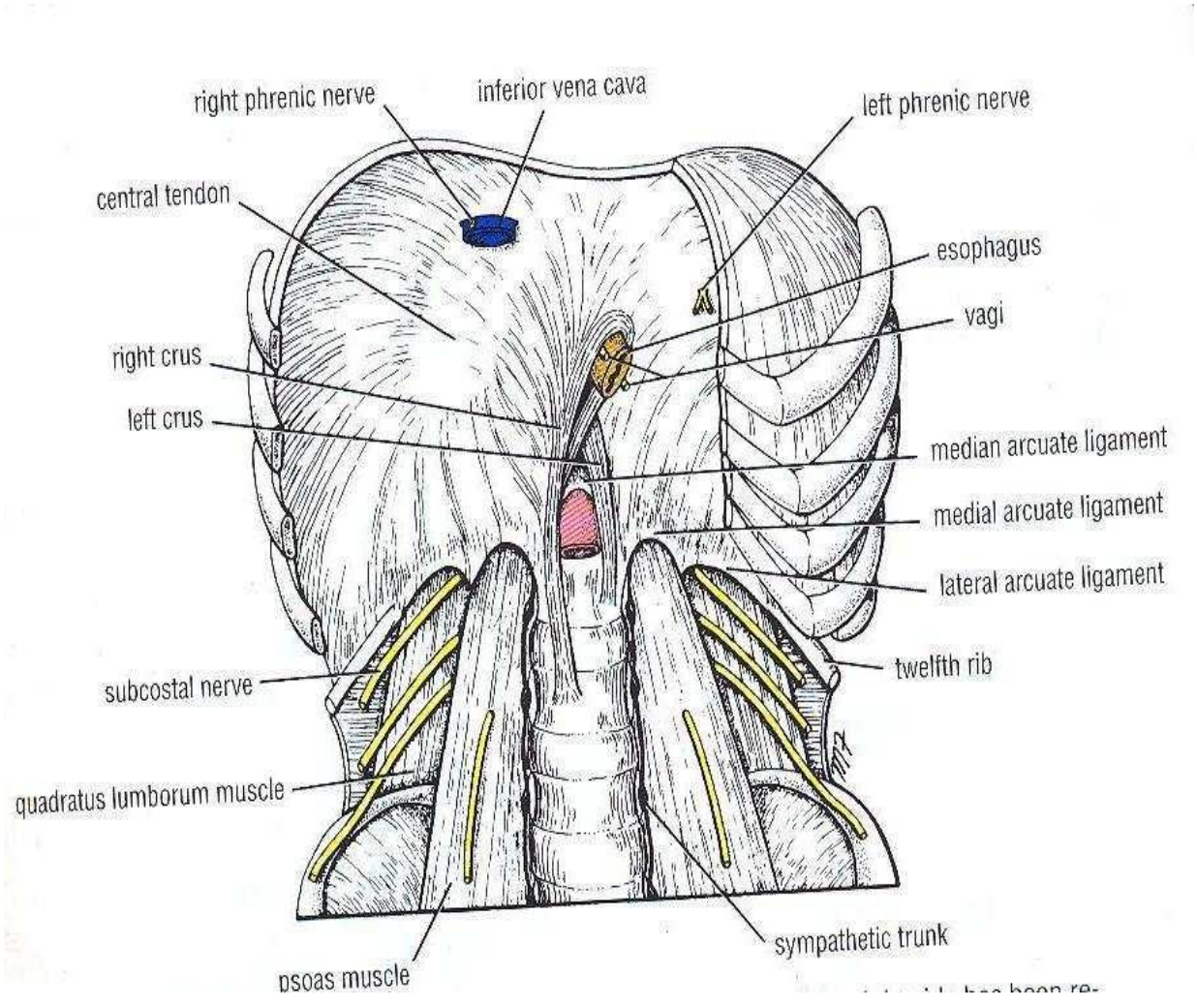

Figure 1-16. Diaphragm as seen from below. The anterior portion of the right side has been removed.

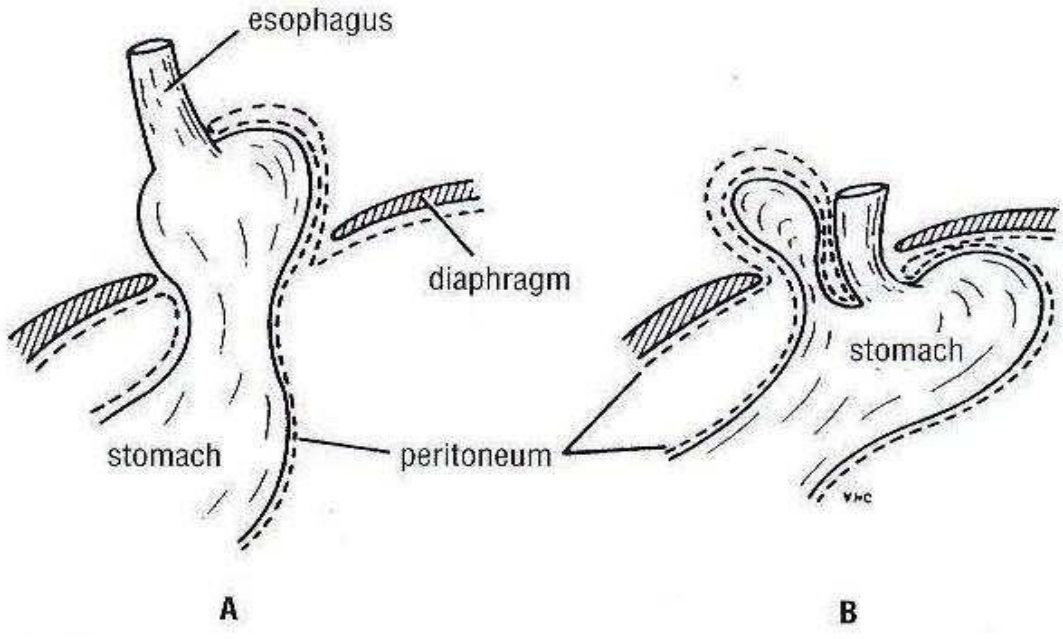

Figure 1-17. A. Sliding esophageal hernia. B. paraesophageal hernia

The internal thoracic artery supplies the anterior wall of the body from the clavicle to the umbilicus. It is a branch of the first part of the subclavian artery in the neck. It descends vertically on the pleura behind the costal cartilages, a fingerbreadth lateral to the sternum, and ends in the sixth intercostal space by dividing into the superior epigastric and musculophrenic arteries (figure 1-10). Two anterior intercostal arteries for the upper six intercostal spaces. Perforating arteries, which accompany the terminal branches of the corresponding intercostal nerves. The pericardiacophrenic artery, which accompanies the phrenic nerve and supplies the pericardium. Mediastinal arteries to the contents of the anterior mediastinum (e.g., the thymus). The superior epigastric artery, which enters the rectus sheath of the anterior abdominal wall and supplies the rectus muscle as far as the umbilicus. The musculophrenic artery, which runs around the costal margin of the diaphragm and supplies the lower intercostal spaces and the diaphragm.

The internal thoracic vein accompanies the internal thoracic artery and drains into the brachiocephalic vein on each side. There are 12 pairs of muscles. Each levator

costa is triangular in shape and arises by its apex from the tip of the transverse process and is inserted into the rib below. Each raises the rib below and is therefore an inspiratory muscle. The serratus posterior superior is a thin, flat muscle that arises from the lower cervical and upper thoracic spines. Its fibers pass downward and laterally and are inserted into the upper ribs. It elevates the ribs and is therefore an inspiratory muscle. The serratus posterior inferior is a thin, flat muscle that arises from the upper lumbar and lower thoracic spines. Its fibers pass upward and laterally and are inserted into the lower ribs. It depresses the ribs and is therefore an expiratory muscle.

The suprasternal notch is the superior margin of the manubrium sterni and is easily felt between the prominent medial ends of the clavicles in the midline (figure 1-18). It lies opposite the lower border of the body of the second thoracic vertebra (Figure 1-2). The sternal angle (angle of Louis) is the angle made between the manubrium and body of the sternum (Figure 1-18). It lies opposite the intervertebral disc between the fourth and fifth thoracic vertebrae (Figure 1-2). The position of the sternal angle can easily be felt and is often seen as a transverse ridge. The finger moved to the right or to the left will pass directly onto the second costal cartilage and then the second rib. All ribs may be counted from this point. Occasionally in a very muscular male, the ribs and intercostal spaces are often obscured by large pectoral muscles. In these cases, it may be easier to count up from the 12th rib. The xiphisternal joint is the joint between the xiphoid process of the sternum and the body of the sternum (Figure 1-19). It lies opposite the body of the ninth thoracic vertebra (Figure 1-2).

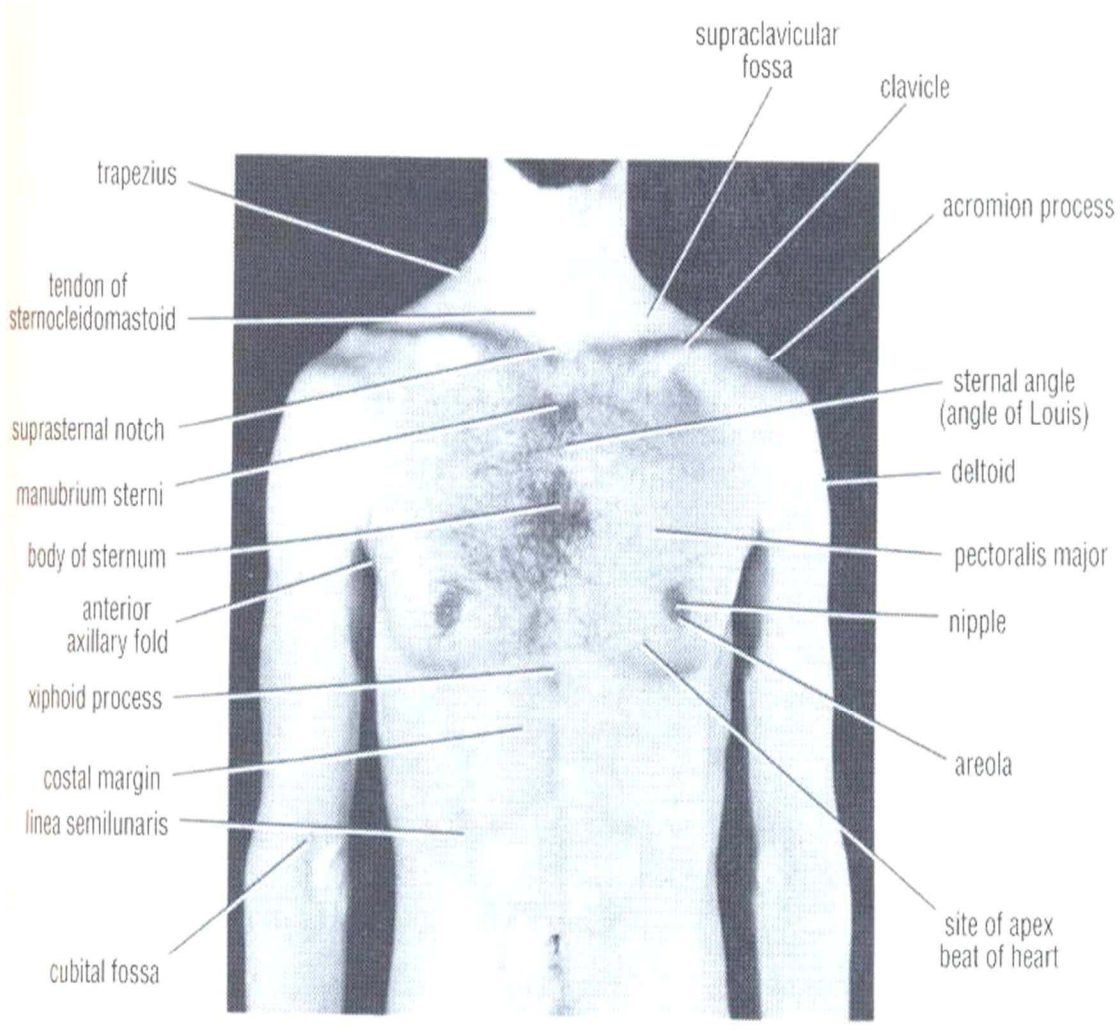

Figure 1-18. Anterior view of thorax of a 27 years old man.

The subcostal angle is situated at the inferior end of the sternum, between the sternal attachments of the seventh costal cartilages (Figure 1-19).

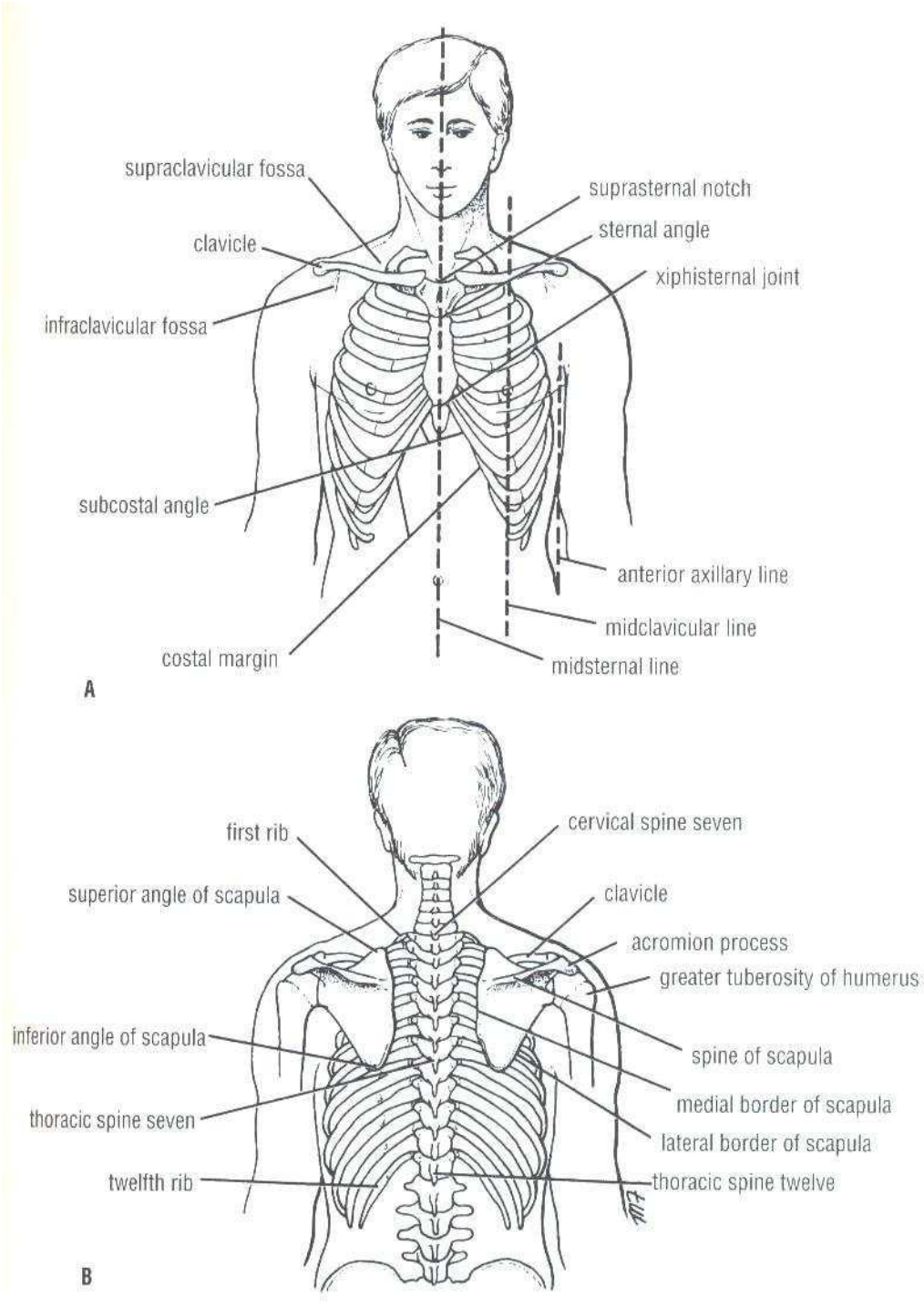

Figure 1-19. Surface landmarks of anterior (A) and posterior (B) thoracic walls.

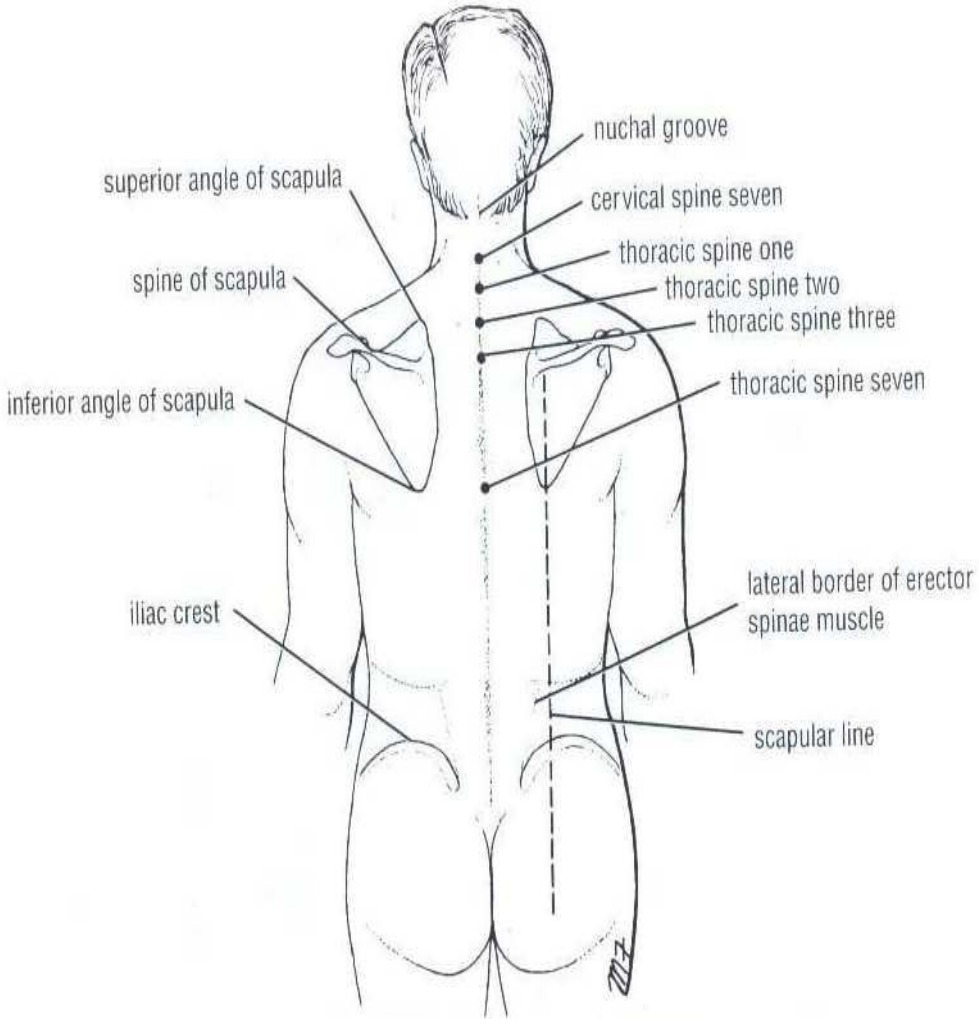

Figure 2-20. Surface landmarks of the posterior thoracic wall

The costal margin is the lower boundary of the thorax and is formed by the cartilages of the 7th, 8th, 9th, and 10th ribs and the ends of the 11th and 12th cartilages (Figure 2-19 and Figure 2-20). The lowest part of the costal margin is formed by the 10th rib and lies at the level of the third lumbar vertebra. The clavicle is subcutaneous throughout its entire length and can be easily palpated (Figure 2-20 and Figure 2-21). It articulates at its lateral extremity with the acromion process of the scapula.

The first rib lies deep to the clavicle and cannot be palpated. The lateral surfaces of the remaining ribs can be felt by pressing the fingers upward into the axilla and

drawing them downward over the lateral surface of the chest wall. The 12th rib can be used to identify a particular rib by counting from below. However, in some individuals, the 12th rib is very short and difficult to feel. For this reason, an alternative method may be used to identify ribs by first palpating the sternal angle and the second costal cartilage. The central tendon of the diaphragm lies directly behind the xiphisternal joint. In the midrespiratory position the summit of the right dome of the diaphragm arches upward as far as the upper border of the fifth rib in the midclavicular line, but the left dome only reaches as far as the lower border of the fifth rib.

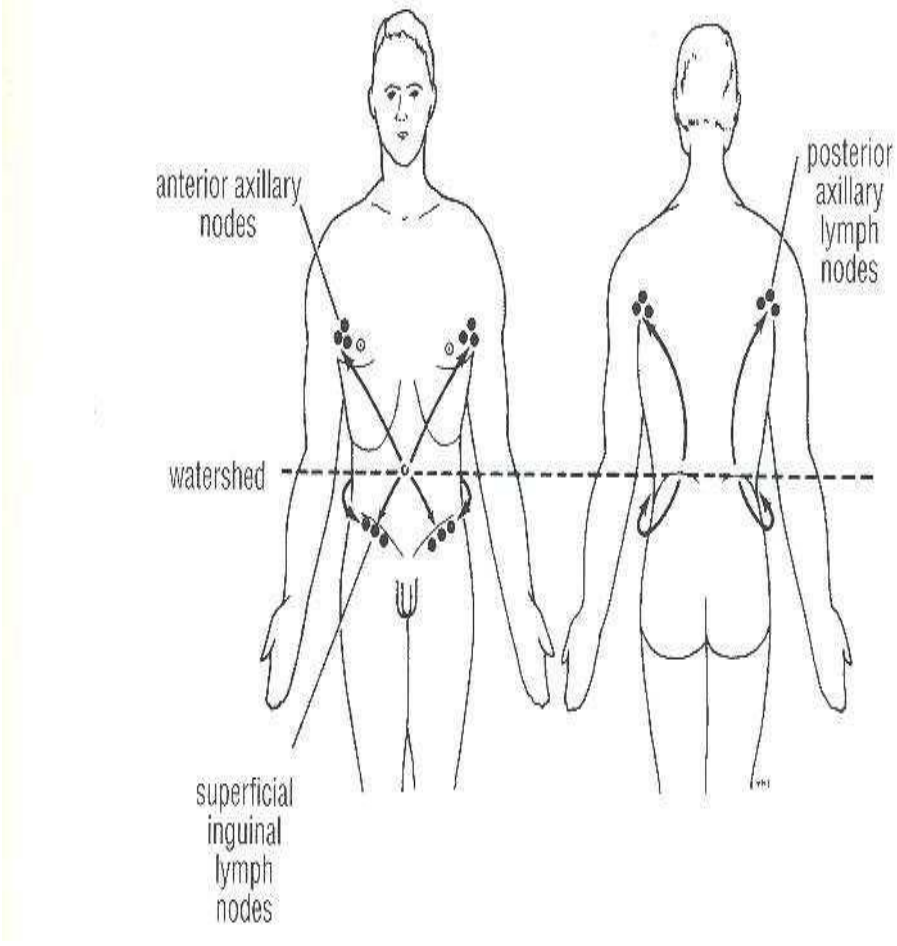

Figure 1-20. Lymph drainage of skin of the skin of thorax and abdomen.

In the male, the nipple usually lies in the fourth intercostal space about 4 in. (10 cm) from the midline. In the female, its position is not constant.

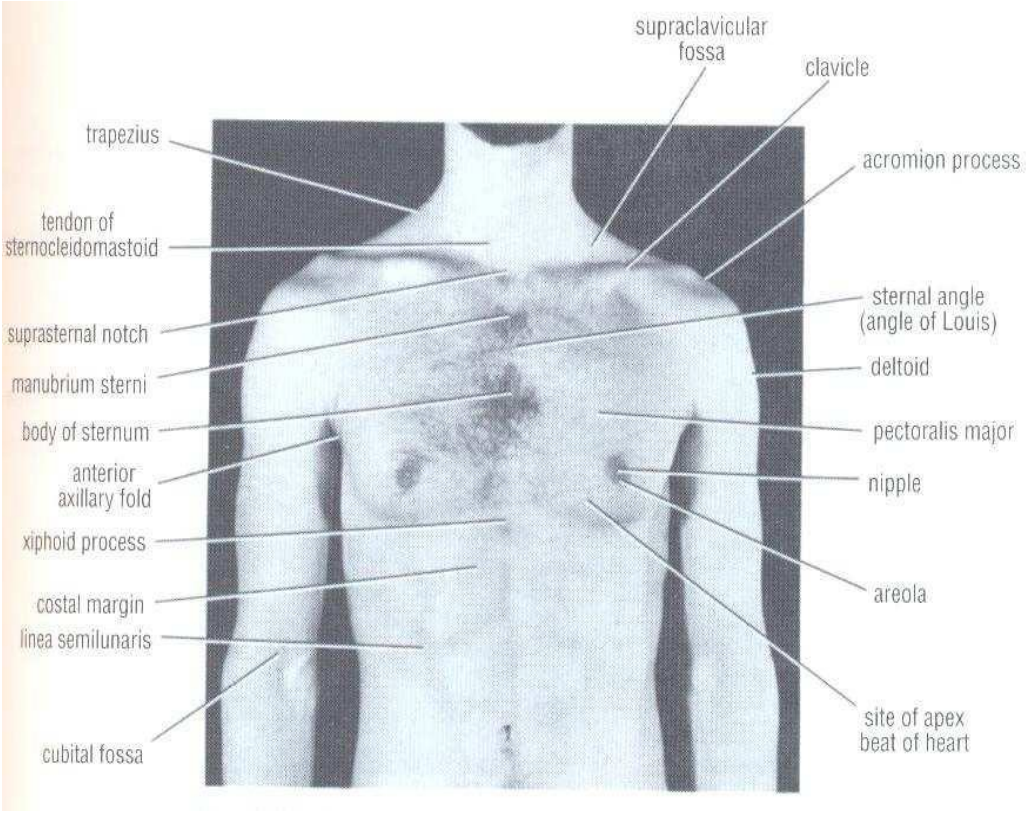

Figure 1-21. Anterior view of the thorax of a 27-years old man

The apex of the heart is formed by the lower portion of the left ventricle. The apex beat is caused by the apex of the heart being thrust forward against the thoracic wall as the heart contracts. (The heart is thrust forward with each ventricular contraction because of the ejection of blood from the left ventricle into the aorta; the force of the blood in the aorta tends to cause the curved aorta to straighten slightly, thus pushing the heart forward.) The apex beat can usually be felt by placing the flat of the hand on the chest wall over the heart. After the area of cardiac pulsation has been determined, the apex beat is accurately localized by placing two fingers over the intercostal spaces and moving them until the point of maximum pulsation is found. The apex beat is normally found in the fifth left intercostal space 3.5 in. (9 cm) from the midline. Should you have difficulty in finding the apex beat, have the patient lean forward in the sitting position. In a

female with pendulous breasts, the examining fingers should gently raise the left breast from below as the intercostal spaces are palpated. The anterior fold is formed by the lower border of the pectoralis major muscle (Figure 2-19 and figure 2-20). This can be made to stand out by asking the patient to press a hand hard against the hip. The posterior fold is formed by the tendon of the latissimus dorsi muscle as it passes around the lower border of the teres major muscle.

The spinous processes of the thoracic vertebrae can be palpated in the midline posteriorly (Figure 1-21). The index finger should be placed on the skin in the midline on the posterior surface of the neck and drawn downward in the nuchal groove. The first spinous process to be felt is that of the seventh cervical vertebrae (vertebra prominens). Below this level are the overlapping spines of the thoracic vertebrae. The spines of C1 to 6 vertebrae are covered by a large ligament, the ligamentum nuchae. It should be noted that the tip of a spinous process of a thoracic vertebra lies posterior to the body of the next vertebra below. The scapula (shoulder blade) is flat and triangular in shape and is located on the upper part of the posterior surface of the thorax. The superior angle lies opposite the spine of the second thoracic vertebra (Figure 1-20 and figure 1-21). The spine of the scapula is subcutaneous, and the root of the spine lies on a level with the spine of the third thoracic vertebra (Figure 2-20 and 2-21). The inferior angle lies on a level with the spine of the seventh thoracic vertebra (Figure 1-20 and figure 1-21). The trachea extends from the lower border of the cricoids cartilage (opposite the body of the sixth cervical vertebra) in the neck to the level of the sternal angle in the thorax (Figure 2-22). It commences in the midline and ends just to the right of the midline by dividing into the right and left principal bronchi. At the root of the neck it may be palpated in the midline in the suprasternal notch. The apex of the lung projects into the neck. It can be mapped out on the anterior surface of the body by drawing a curved line, convex upward,

from the sternoclavicular joint to a point 1 in. (2.5 cm) above the junction of the medial and intermediate thirds of the clavicle (Figure 1-22). The anterior border of the right lung begins behind the sternoclavicular joint and runs downward, almost reaching the midline behind the sternal angle. It then continues downward until it reaches the xiphisternal joint (Figure 1-23). The anterior border of the left lung has a similar course, but at the level of the fourth costal cartilage it deviates laterally and extends for a variable distance beyond the lateral margin of the sternum to form the cardiac notch (Figure 1-23). This notch is produced by the heart displacing the lung to the left. The anterior border then turns sharply downward to the level of the xiphisternal joint.

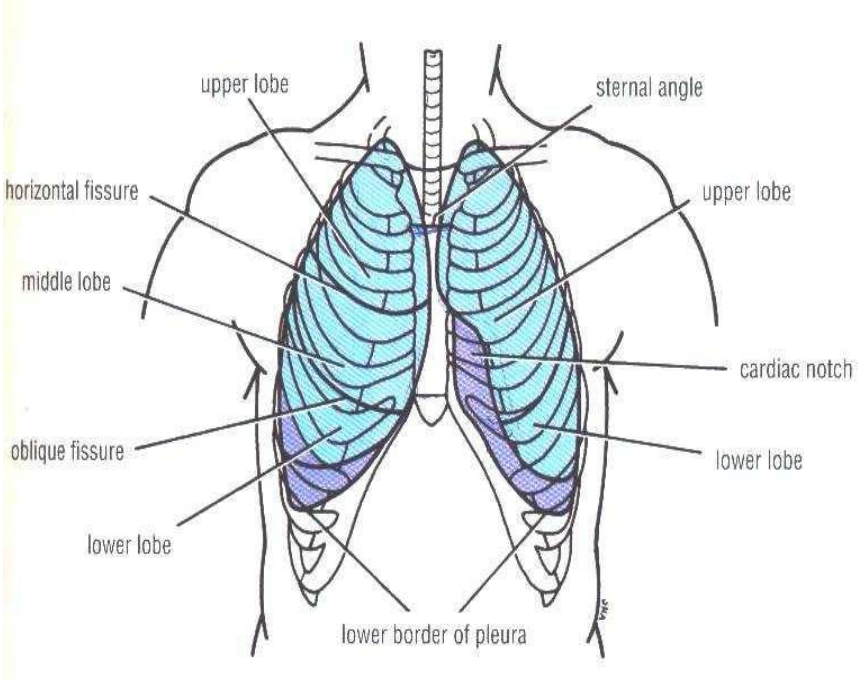

Figure 1-22. Surface markings of lungs and parietal pleura on the anterior thoracic wall

The lower border of the lung in midinspiration follows a curving line, which crosses the 6th rib in the midclavicular line and the 8th rib in the midaxillary line, and reaches the 10th rib adjacent to the vertebral column posteriorly (Figure 1-23). It is important to understand that the level of the inferior. The posterior

border of the lung extends downward from the spinous process of the 7th cervical vertebra to the level of the 10th thoracic vertebra and lies about 1.5 in. (4 cm) from the midline (Figure 1-23). The oblique fissure of the lung can be indicated on the surface by a line drawn from the root of the spine of the scapula obliquely downward, laterally and anteriorly, following the course of the sixth rib to the sixth costochondral junction. In the left lung the upper lobe lies above and anterior to this line; the lower lobe lies below and posterior to it (Figure 1-23). In the right lung is an additional fissure, the horizontal fissure, which may be represented by a line drawn. Horizontally along the fourth costal cartilage to meet the oblique fissure in the midaxillary line (Figure 1-23 and figure 1-24). Above the horizontal fissure lies the upper lobe and below it lies the middle lobe; below and posterior to the oblique fissure lies the lower lobe.

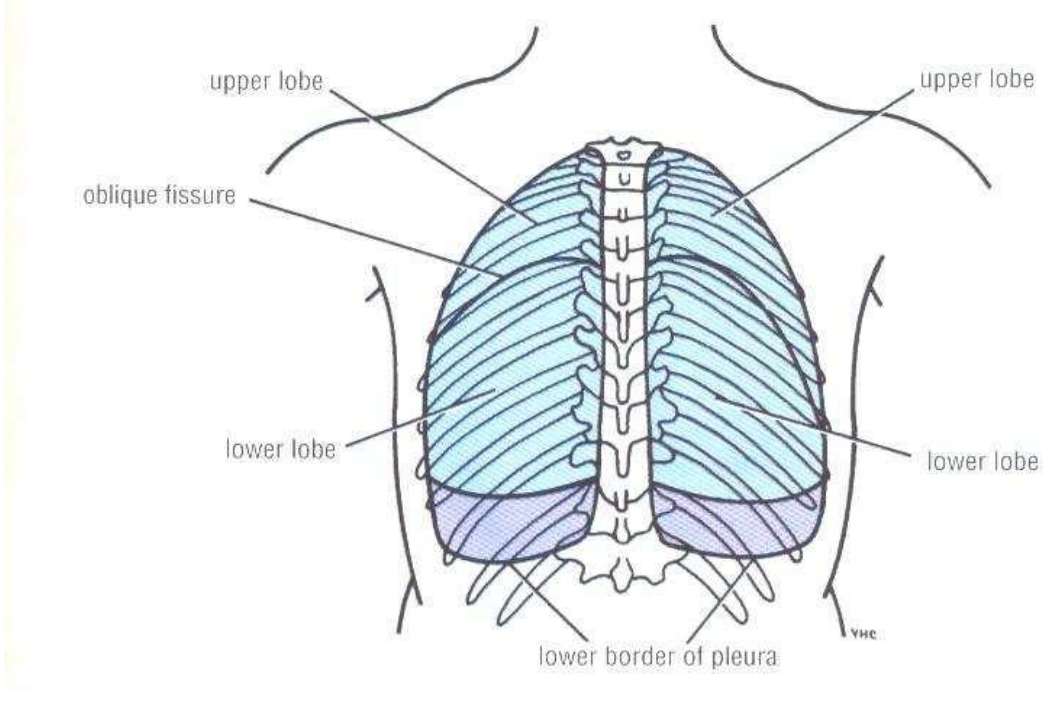

Figure 1-23. Surface markings of the lungs and parietal pleura on the posterior thoracic wall.

The boundaries of the pleural sac can be marked out as lines on the surface of the body. The lines, which indicate the limits of the parietal pleura where it lies close

to the body surface, are referred to as the lines of pleural reflection. The cervical pleura bulges upward into the neck and has a surface marking identical to that of the apex of the lung. A curved line may be drawn, convex upward, from the sternoclavicular joint to a point 1 in. (2.5 cm) above the junction of the medial and intermediate thirds of the clavicle (Figure 1-24). The anterior border of the right pleura runs down behind the sternoclavicular joint, almost reaching the midline behind the sternal angle. It then continues downward until it reaches the xiphisternal joint. The anterior border of the left pleura has a similar course, but at the level of the fourth costal cartilage it deviates laterally and extends to the lateral margin of the sternum to form the cardiac notch. (Note that the pleural cardiac notch is not as large as the cardiac notch of the lung.) It then turns sharply downward to the xiphisternal joint (Figure 1-24). The lower border of the pleura on both sides follows a curved line, which crosses the 8th rib in the midclavicular line and the 10th rib in the midaxillary line, and reaches the 12th rib adjacent to the vertebral column that is, at the lateral border of the erector spinae muscle (Figure 2-24). Note that the lower margins of the lungs cross the 6th, 8th, and 10th ribs at the midclavicular lines, the midaxillary lines, and the sides of the vertebral column, respectively; the lower margins of the pleura cross, at the same points, the 8th, 10th, and 12th ribs, respectively. The distance between the two borders corresponds to the costodiaphragmatic recess.

1.2.1. The Thoracic Cavity

The chest cavity is bounded by the chest wall and below by the diaphragm. It extends upward into the root of the neck about one fingerbreadth above the clavicle on each side (Figure 1-25). The diaphragm, which is a very thin muscle, is the only structure (apart from the pleura and peritoneum) that separates the chest from the abdominal viscera. The chest cavity can be divided into a median

partition, called the mediastinum, and the laterally placed pleurae and lungs (Figure 1-26, Figure 127, and figure 1-28).

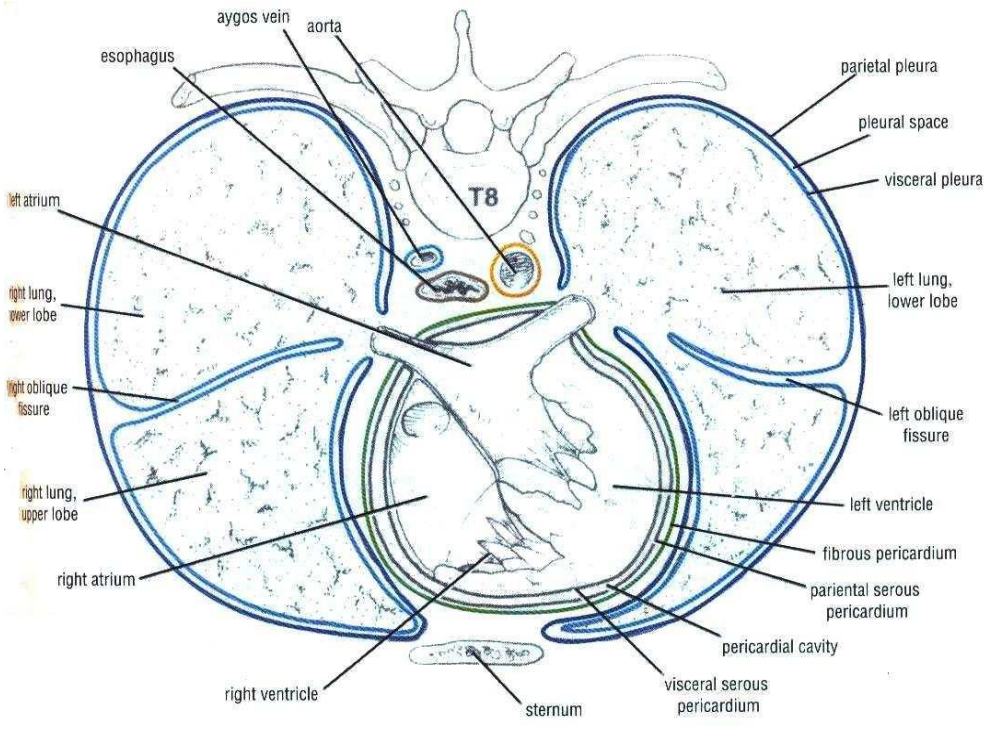

Figure 2-26. Cross section of the thorax at the level of eighth thoracic vertebrae.

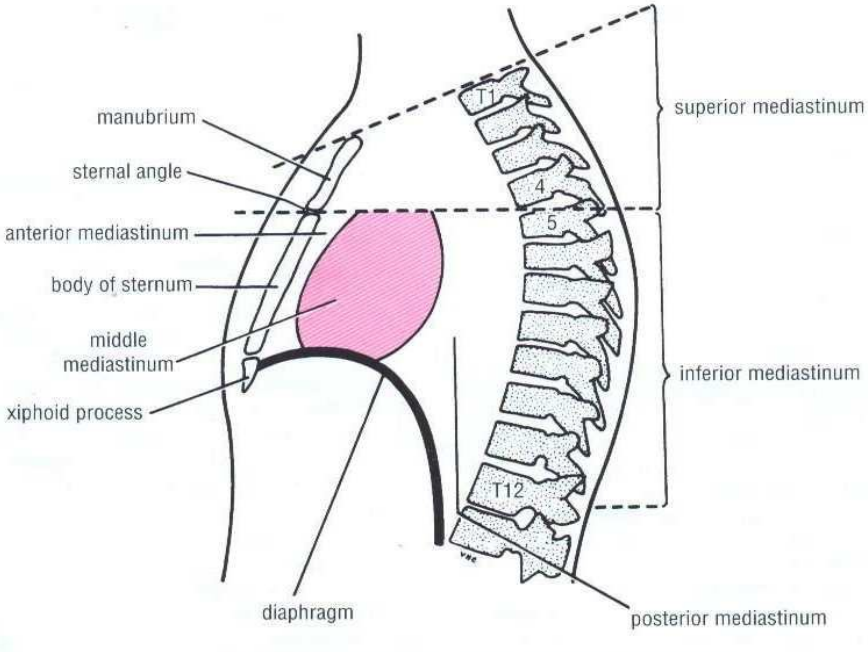

Figure 3-2 Subdivisions of the mediastinum.

Figure 1-27. Subdivisions of the mediastinum

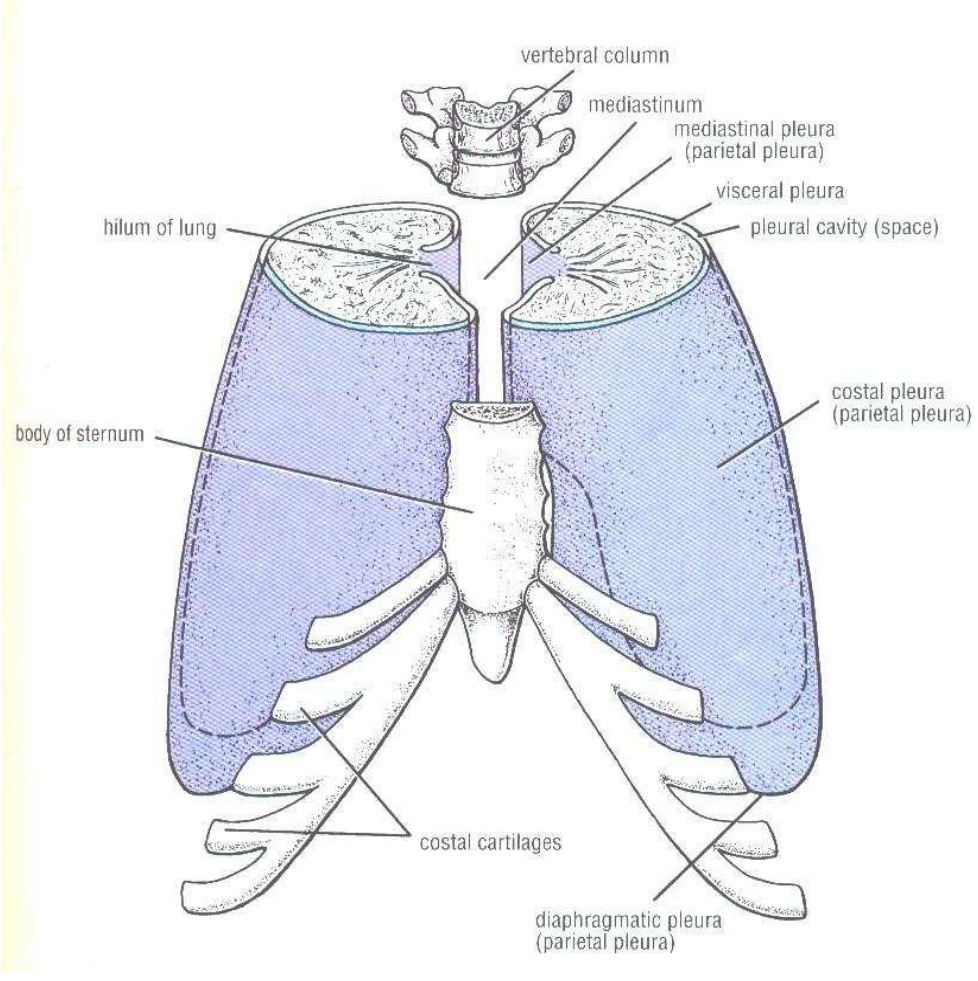

Figure 1-28. Pleurae from above and in front

The mediastinum, though thick, is a movable partition that extends superiorly to the thoracic outlet and the root of the neck and inferiorly to the diaphragm. It extends anteriorly to the sternum and posteriorly to the vertebral column. It contains the remains of the thymus, the heart and large blood vessels, the trachea and esophagus, the thoracic duct and lymph nodes, the vagus and phrenic nerves, and the sympathetic trunks. The mediastinum is divided into superior and inferior mediastina by an imaginary plane passing from the sternal angle anteriorly to the lower border of the body of the fourth thoracic vertebra posteriorly (Figure 1-29 a& b). The inferior mediastinum is further subdivided into the middle

mediastinum, which consists of the pericardium and heart; the anterior mediastinum, which is a space between the pericardium and the sternum; and the posterior mediastinum, which lies between the pericardium and the vertebral column.

For purposes of orientation, it is convenient to remember that the major mediastinal structures are arranged in the following order from anterior to posterior.

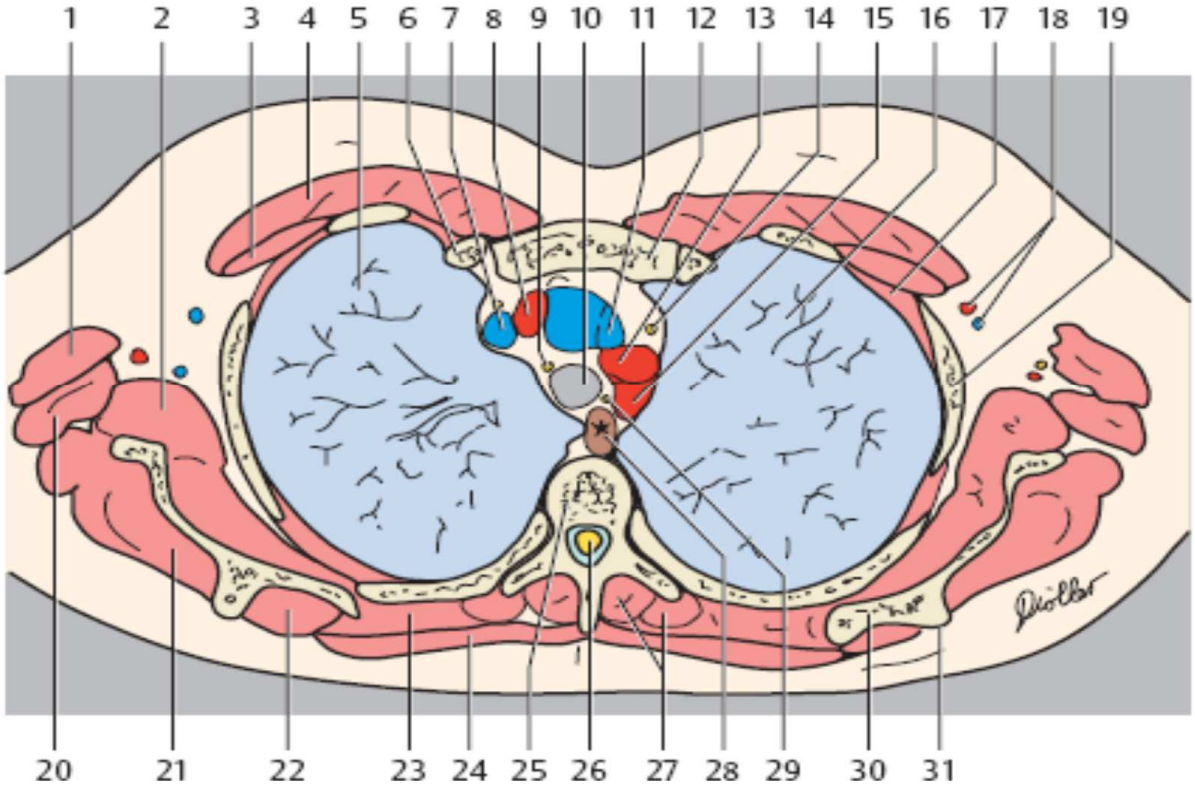

1. Deltoid muscle
2. Subscapularis muscle
3. Pectoralis minor muscle
4. Pectoralis major muscle
5. Right lung
6. Rib
7. Right brachiocephalic vein
8. Right brachiocephalic artery
9. Vagus nerve
10. Trachea
11. Left brachiocephalic vein
12. Sternum (manubrium)
13. Left common carotid artery
14. Phrenic nerve
15. Left subclavian artery
16. Left lung
17. Intercostal muscle
18. Axillary artery and vein
19. Rib
20. Teres major muscle and latissimus dorsi muscle
21. Infraspinatus muscle
22. Supraspinatus muscle
23. Rhomboid muscle major
24. Trapezius muscle
25. Thoracic vertebra
26. Spinal cord (thoracic part)
27. Erector spinae muscle
28. Esophagus
29. Recurrent laryngeal nerve
30. Scapula
31. Spine of scapula
32. Superficial axillary lymph nodes
33. Interpectoral lymph nodes
34. Paravertebral lymph nodes
35. Paratracheal lymph nodes
36. Anterior mediastinal lymph nodes
37. Parasternal lymph nodes
38. Paraesophageal lymph nodes
39. Intercostal lymph nodes

(a)

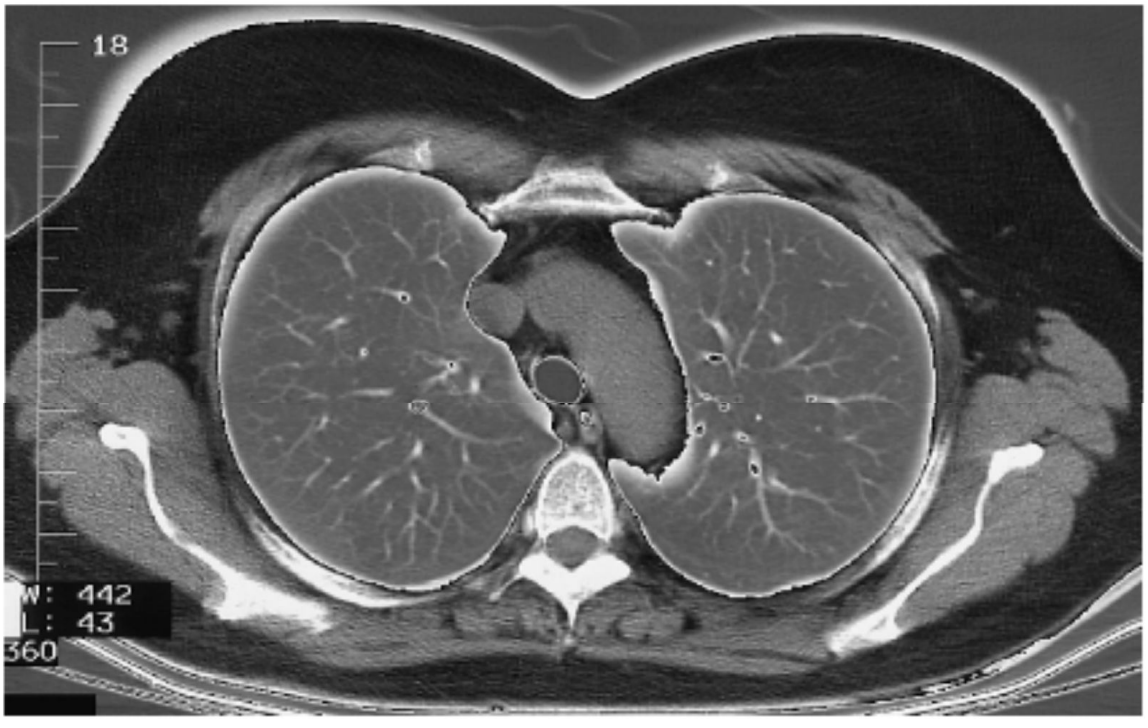

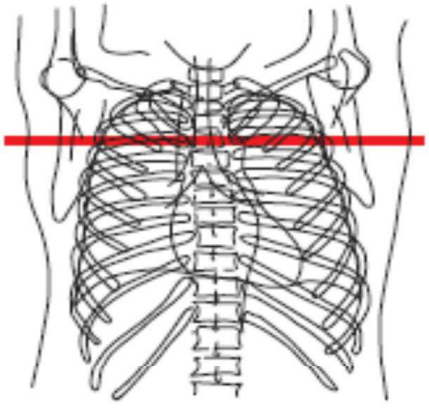

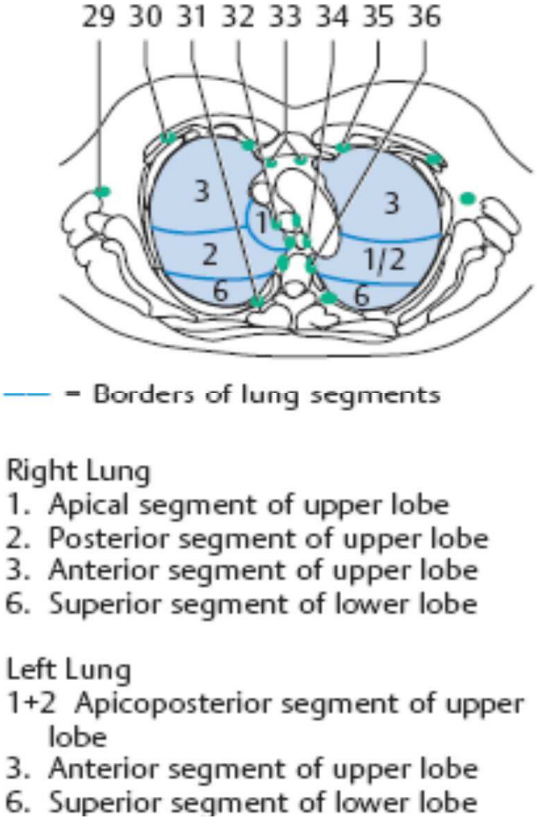

(b)

Figure 1-29. Show Ct image thorax Cavity (a) Gross anatomy (b) cross sectional Anatomy

1.3. Target volume definition

A common international language for describing target volumes is found in International Commission on Radiation Units (ICRU) published recommendations Report 50 (1993), 62 (1999) and 71 (2004). These contain clear definitions (Figure1.30) to enable centers to use the same criteria for delineating tumors for radiation so that their treatment results can be compared.

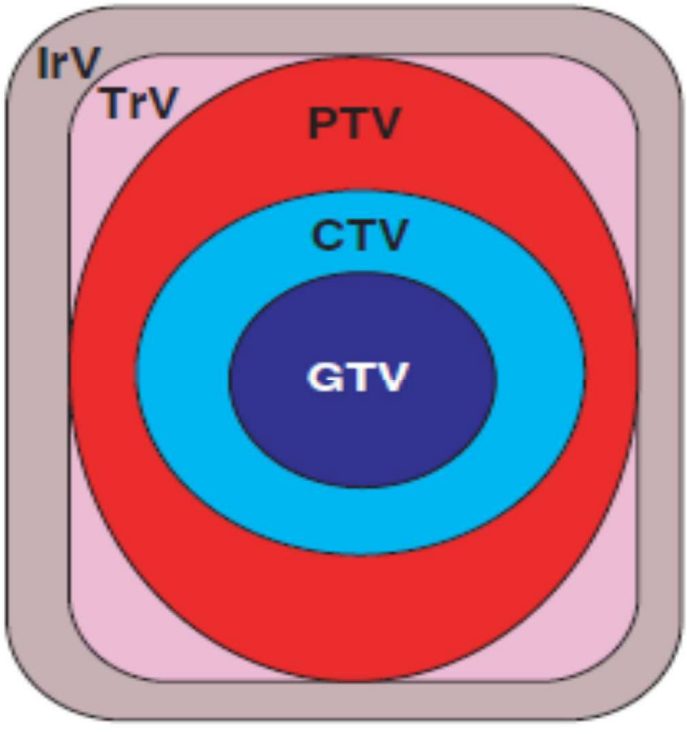

Figure 1.30. ICRU target volume definitions showing GTV, CTV, PTV, treated and irradiated volume. Reproduced with permission from ICRU (1993) Prescribing, Recording and Reporting Photon Beam Therapy. ICRU report 50.

Gross tumor volume (GTV) is the primary tumor or other tumor mass shown by clinical examination, at examination under anaesthetic (EUA) or by imaging. GTV is classified by staging systems such as TNM (UICC), AJCC or FIGO. Tumor size, site and shape may appear to vary depending on the imaging technique used and an optimal imaging method for each particular tumor site must therefore also be specified. A GTV may consist of primary tumor (GTV-T)

and/or metastatic lymphadenopathy (GTV-N) or distant metastases (GTV-M). GTV always contains the highest tumor cell density and is absent after complete surgical resection.

Clinical target volume (CTV) contains the GTV when present and/or subclinical microscopic disease that has to be eradicated to cure the tumor. CTV definition is based on histological examination of post mortem or surgical specimens assessing extent of tumor cell spread around the gross GTV, as described by Holland et al. (1985) for breast cancer. The GTV-CTV margin is also derived from biological characteristics of the tumor, local recurrence patterns and experience of the radiation oncologist. A CTV containing a primary tumor may lie in continuity with a nodal GTV/CTV to create a CTV-TN (e.g. tonsillar tumor and ipsilateral cervical nodes). When a potentially involved adjacent lymph node which may require elective irradiation lies at a distance from the primary tumor, separate CTV-T and CTV-N are used (Figure 1.31), e.g. an anal tumor and the inguinal nodes.

CTV can be denoted by the dose level prescribed, as for example, CTV-T50 for a particular CTV given 50 Gy. For treatment of breast cancer, three CTVs may be used for an individual patient: CTV-T50 (50 Gy is prescribed to the whole breast); CTV-T66 (66 Gy to the tumor bed); and CTV-N50 (50 Gy to regional lymph nodes). Variation in CTV delineation by the clinician (‘doctor's delineation error’) is the greatest geometrical uncertainty in the whole treatment process.

Studies comparing outlining by radiologists and oncologists have shown a significant inter-observer variability for both the GTV and/or CTV at a variety of tumor sites. This is greater than any intra-observer variation. Published results for nasopharynx, brain, lung, prostate, medulloblastoma and breast all show significant discrepancies in the volumes outlined by different clinicians. Improvements can be made with training in radiological anatomy which enables

clinicians to distinguish blood vessels from lymph nodes and to identify structures accurately on computed tomography (CT) and magnetic resonance imaging (MRI). Joint outlining by radiologists and oncologists can improve consistency and ensure accurate interpretation of imaging of the GTV. Consensus guidelines such as those for defining CTV for head and neck nodes (Gregoire et al. 2000) and pelvic nodes (Taylor et al. 2005) have improved CTV delineation greatly.

When the patient moves or internal organs change in size and shape during a fraction of treatment or between fractions (intra- or inter-fractionally), the position of the CTV may also move. Therefore, to ensure a homogeneous dose to the CTV throughout a fractionated course of irradiation, margins must be added around the CTV. These allow for physiological organ motion (internal margin) and variations in patient positioning and alignment of treatment beams (set-up margin), creating a geometric planning target volume. The planning target volume (PTV) is used in treatment planning to select appropriate beams to ensure that the prescribed dose is actually delivered to the CTV. Variations in organ motion may be small (e.g. brain), larger and predictable (e.g. respiration or cardiac pulsation), or unpredictable (e.g. rectal and bladder filling).

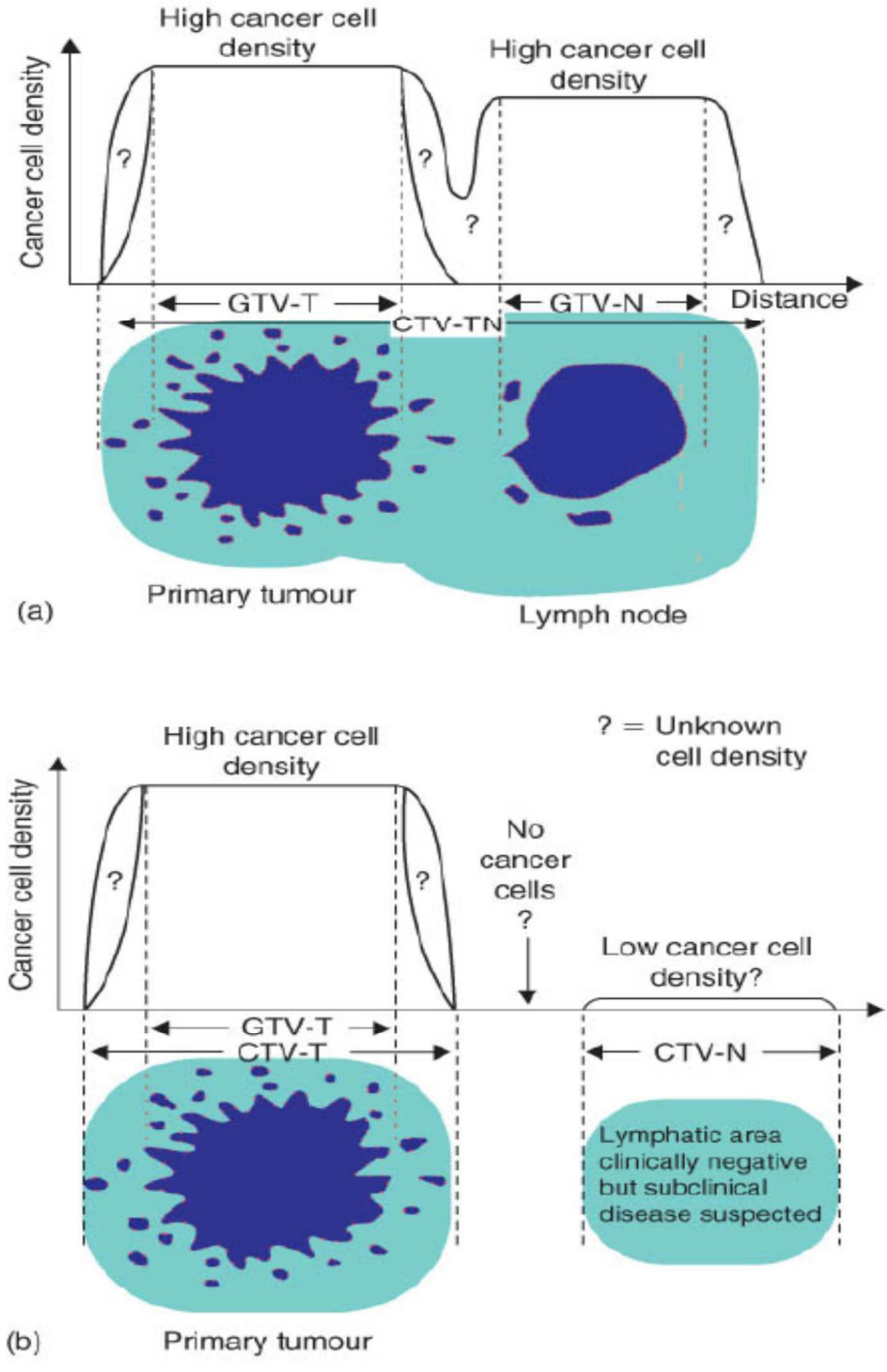

Figure 1.31. ICRU illustrations to show (a) GTV-T plus GTV-N in continuity (CTV-TN) and (b) CTV-T and CTV-N at a distance. Reproduced with permission from ICRU (2004) Prescribing, Recording and Reporting Electron Beam Therapy. ICRU report 71.

When treating lung tumors, the displacement of the CTV caused by respiration can be dealt with in several ways: by increasing the CTV-PTV margin

eccentrically to include all CTV positions during a respiratory cycle; by using suspended respiration with a technique such as the active breathing control (ABC) device; or by delivery of radiation using gating or respiratory correlated CT scanning and treatment. Uncertainties from organ motion can also be reduced by using fiducial markers, and published results are available for lung, prostate and breast tumors.

Radio-opaque markers are inserted and imaged at localization using CT or MRI, and at treatment verification, using portal films, electronic portal imaging devices (EPIDs) or online cone beam CT image-guided radiotherapy (IGRT). The internal margin therefore allows for inter- and intra-fractional variations in organ position and shape which cannot be eliminated.

The treated volume is the volume of tissue that is planned to receive a specified dose and is enclosed by the isodose surface corresponding to that dose level, e.g. 95 percent. The shape, size and position of the treated volume in relation to the PTV should be recorded to evaluate and interpret local recurrences (in field versus marginal) and complications in normal tissues, which may be outside the PTV but within the treated volume.

The irradiated volume is the volume of tissue that is irradiated to a dose considered significant in terms of normal tissue tolerance, and is dependent on the treatment technique used. The size of the irradiated volume relative to the treated volume (and integral dose) may increase with increasing numbers of beams, but both volumes can be reduced by beam shaping and conformal therapy. The organs at risk are critical normal tissues whose radiation sensitivity may significantly influence treatment planning and/or prescribed dose. Any movements of the organs at risk (OAR) or uncertainties of set-up may be accounted for with a margin similar to the principles for PTV, to create a planning organ at risk volume (PRV).

The size of the margin may vary in different directions. Where a PTV and PRV are close or overlap a clinical decision about relative risks of tumor relapse or normal tissue damage must be made. Shielding of parts of normal organs is possible with the use of multi-leaf collimation (MLC). Dose–volume histograms (DVHs) are used to calculate normal tissue dose distributions.

1.4. Set-up variations/set-up margin

During a fractionated course of radiotherapy, variations in patient position and in alignment of beams will occur both intra- and inter-fractionally, and a margin for set-up error must be incorporated into the CTV-PTV margin. Errors may be systematic or random. Systematic errors may result from incorrect data transfer from planning to dose delivery, or inaccurate placing of devices such as compensators, shields, etc. Such systematic errors can be corrected. Random errors in set-up may be operator dependent, or result from changes in patient anatomy from day to day which are impossible to correct. Accuracy of set-up may be improved with better immobilization, attention to staff training and/or implanted opaque fiducial markers, such as gold seeds, whose position can be determined in three dimensions at planning, and checked during treatment using portal imaging or IGRT. Translational errors can thereby be reduced to 1 mm and rotational errors to 1°. Each department should measure its own systematic and random errors for each treatment technique by comparing portal imaging and digitally reconstructed radiographs (DRRs). These measurements are then incorporated into the CTVPTV margin using the formula devised by Van Herk, where the CTV is covered for 90 per cent of the patients with the 95 per cent isodoses:

$$\textbf{PTV margin} = 2.5\Sigma + 0.74\sigma$$

where Σ = total standard deviation (SD) computed as the square root of the sum of the squared individual SD values of all systematic errors for organ motion and

setup; and σ= total SD of all random errors combined quadratically in a similar way.

This provides a population-derived standard CTV-PTV margin for a particular technique in a given centre and can be non-isotropic in craniocaudal, transverse and anteroposterior (AP) directions. Accurate treatment delivery depends on reducing or eliminating systematic errors and requires a high level of awareness of all staff throughout the many different work areas from localization through to treatment. Other theories about how to incorporate organ motion and the uncertainty of the 'mean' position of the CTV on a snapshot CT scan used for localization have been proposed. Van Herk suggests a volume large enough to contain the mean position of the CTV in 90 per cent of cases, called the systematic target volume (STV). Collection of data on the precise CT location of tumor recurrences in relation to the original target volume is important to improve margin definition.

1.5. The problem:

The most important criterion of Radiology images is enhancement and resolution to differentiate between two or more closely localized issues. The main problem of CT images is to find better estimates for the noise variance in those images. The motivation comes from the experience, which simplifying assumption of independently identically Distributes (IID) noise statistics, this may lead to an error in estimation of noise variances. Thus, in real x-rays images can find s significant coherence of the noise with the image contents.

1.6. Objectives

The main objective of this research is to study automatic data extraction in computed tomography images using morphology matching filtering.

1.6.1. Specific objectives

- To evaluate contrast enhancement pattern in different computed tomography images such as grey color.
- To evaluate the usage of new nonlinear approach for contrast enhancement of soft tissues in computed tomography images.
- To study automatic extraction of lung tissue in computed tomography

1.7. Overview of study

This study consist of five chapters. Chapter one is introduction .chapter two consists of two parts; part one consist of definition of target volume in radiotherapy, Radiotherapy detection using CT planning system , Image processing using in detection of tumor, MatLab usage in radiotherapy. Part two consists of previous study. Chapter three is materials and methods .chapter four is results. Chapter five is discussion, conclusion and Recommendations.

Chapter Two
Literature Review

2.1. Problems of respiratory motion detection during radiotherapy:

If respiratory motion is not accounted for, as is the case when conventional radiotherapy techniques are applied in thoracic and abdominal sites, it causes artifacts during image acquisition. These artifacts cause distortion of the target volume and incorrect positional and volumetric information. These motion artifacts occur because different parts of the object move in and out of the computed tomography (CT) slice window during image acquisition. Artifacts can be generated within a slice, since CT reconstruction algorithms assume that the imaged anatomy is invariant during data acquisition (Chen et al 2004).

Motion artifacts are commonly seen with thoracic CT images. An example of the difference between a respiratory-gated and a non-gated CT scan for a patient and a sinusoidally moving sphere is shown in Figures 1 and figure 2, respectively.

Artifacts from CT scans manifest themselves as target/normal tissue delineation errors and adversely affect dose-calculation accuracy. It is important to note that respiratory motion can generate artifacts for all imaging modalities, including positron emission tomography (PET) scanning which is becoming a standard-of care imaging technique for NSCLC (Caldwell et al 2003).

If not accounted for, tumor motion will further blur the PET image, leading to difficulties in clearly delineating boundaries as well as failure to detect small mobile volumes that are potentially cancerous (Nehmeh et al 2003).

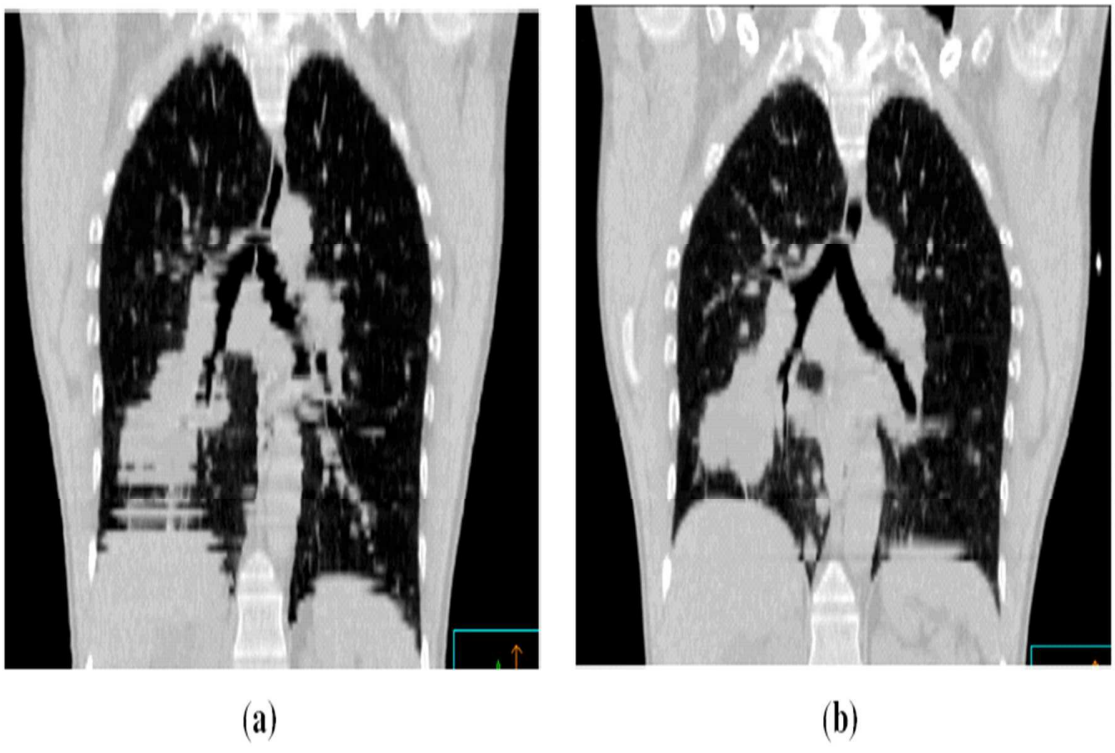

Figure 2-1. Coronal views of CT scans of the same patient taken during free breathing (FB) (a) and with respiratory-gated scanning exhale (b) (Keall et al 2002)

During treatment planning, margins need to be large enough to ensure coverage of the target for most of the treatment delivery. Generally, for CT-planned lung cancer treatments, the GTV is outlined, and a margin is added to include the suspected microscopic spread (which when added to the GTV creates the CTV). Thus, using International Commission on Radiation Units and Measurements (ICRU) report 62 nomenclature, to obtain the planning target volume (PTV) from the CTV involves the addition of the margins to account for intrafraction motion (due to respiration), interfraction motion, and setup error (Giraud et al 2000). Accounting for respiratory motion by adding treatment margins to cover the limits of motion of the tumor is suboptimal, because this increases the radiation field size and consequently the volume of healthy tissues exposed to high doses.

This increased treatment volume increases the likelihood of treatment-related complications (Stevens et al 2001).

However, if the margins are not sufficiently large, part of the CTV will not receive adequate dose coverage. Because of the artifacts observed in CT images in which respiratory motion has not been accounted for, the magnitude of margin to allow for respiratory motion is difficult to quantify, particularly for individual patients in whom a wide range of tumor motion is observed (Seppenwoolde et al 2002).

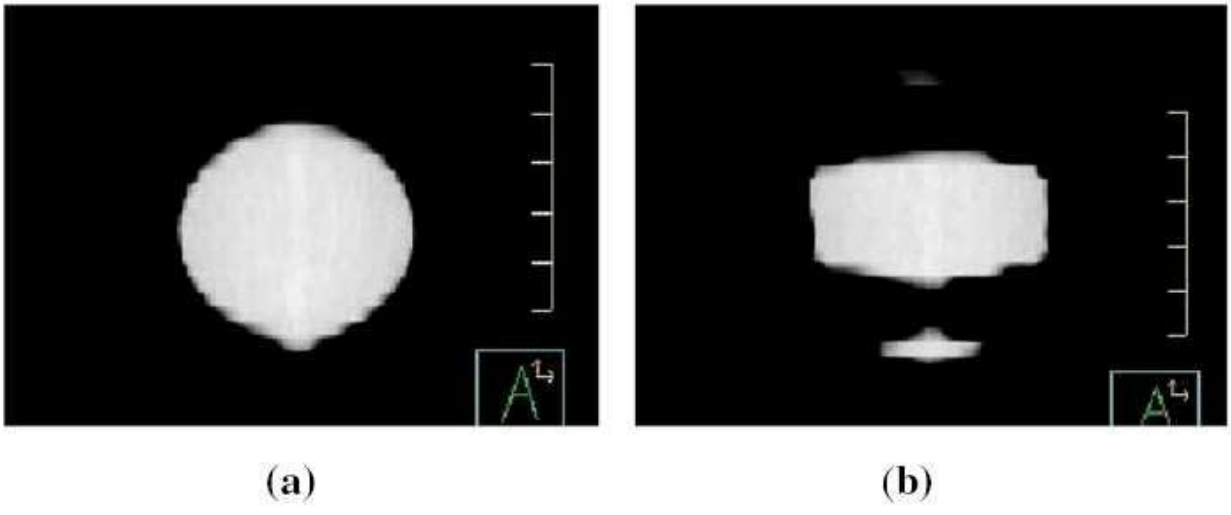

Figure 2-2. Coronal views of CT scan of a static sphere (a) and a sinusoidally moving sphere (b) (2-cm range of motion and a 4-second period). (Vedam et al 2003)

Radiation delivery in the presence of intrafraction organ motion causes an averaging or blurring of the static dose distribution over the path of the motion.

This displacement results in a deviation between the intended and delivered dose distributions. Assuming a static beam, the total positional error affecting the dose is the composite vector of internal (e.g., tumor-bone) and external (bone-treatment room) displacements. Thus, for conventional (non-IMRT) treatments, in which the dose gradient in the center of each field can be assumed to be fairly

small, the effect is manifested by a blurring of the dose distribution by the anatomy moving near the beam edges, in effect increasing the beam penumbra. This effect is thought to be exacerbated during IMRT delivery, causing motion artifacts in dose distribution due to the interplay between motion of the leaves of a multileaf collimator (MLC) and the component of target motion perpendicular to the beam (Malone et al 2000).

2.2. Magnitude and measurement of respiratory motion:

2.1.1. The mechanics of breathing:

The primary function of the lung is to facilitate gas (O_2 and CO_2) exchange between blood and air, thus maintaining normal levels of gas pressure (partial pressure of oxygen, PO_2, and partial pressure of carbon dioxide, PCO_2), in the arterial blood. Respiration is an “involuntary” action; i.e., a person would continue to breathe despite being unconscious. However, within limits, individuals are capable of controlling the frequency and displacement magnitude of their respiration as well as breath-holds. Unlike cardiac motion, the respiratory motion is not rhythmic. The periodic cycle of respiration is regulated through chemoreceptors by the levels of CO_2, O_2, and pH in the arterial blood. Of these, the most important is PCO_2. Reducing PCO_2, as occurs with hyperventilation, is a very effective means for reducing the urge to breathe, or sustaining a breath-hold. Under normal conditions, the O_2 and blood pH stimuli play a small role in ventilation control (Oetzel et al 2005).

Anatomically, the lungs are held within the thoracic cavity, encased by the liquid-filled intrapleural space. Inhalation requires active participation of respiration muscles. During the inhalation part of quiet breathing, the increasing volume of the thoracic cavity draws air into the cavity. The most important muscle of inhalation is the diaphragm. As the diaphragm is contracted, it descends and the abdomen is forced inferiorly and anteriorly, increasing the superior–inferior (SI)

dimension of the chest cavity. The intercostal muscles connect adjacent ribs and also participate in normal inhalation. They contract during inhalation, pulling the ribs superiorly and anteriorly, thereby increasing both the lateral and anterior–posterior (AP) diameters of the thorax, as shown in Figure 2-3. Exhalation is passive for quiet breathing. The lung and chest walls are elastic and return passively to their pre-inhalation positions at exhale. Other ventilation muscles are involved only during active exhalation. The tendency of the lung to recoil to its deflated volume is opposed by the tendency of the chest cage to bow out. The lung volume at the end of exhale, termed "functional residual capacity," is at equilibrium or in the most relaxed state. Typically, the time taken to breathe in is longer than the time taken to breathe out. Transpulmonary pressure, the pressure difference between respired gas at the mouth and the pleural pressure around the lungs, is reduced during inhalation and is recovered during exhalation. During normal breathing, the deflating lung volume is larger than the inflating volume at the same transpulmonary pressure. This is called hysteresis, attributable to the complex respiratory pressure volume relationship of the lung and chest wall (Weiss et al 2003).

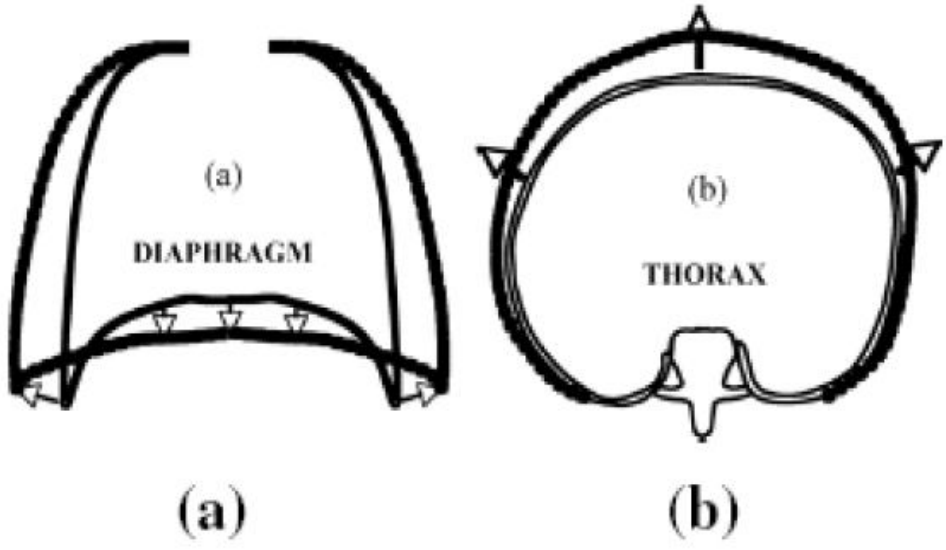

Figure 2-3. (a) During inhalation, the diaphragm contracts, the abdomen is forced down and forward, and the rib cage is lifted. (b) The intercostal muscles also contract to pull and rotate the ribs, resulting in increasing both the lateral and anterior–posterior (AP) diameters of the thorax. (West, 1997)

Breathing pattern characterization measurements have been distinguished by posture (upright, prone, supine, lateral decubitus), breathing type (chest or abdominal), and depth of respiration (shallow, normal, deep). For example, when the change in abdominal circumference was more than 10 mm greater than the change in chest circumference, Davies et al. (1994) classified the breath as abdominal. During normal quiet respiration, the lung volume typically changes by 10% to 25%; at deep inhale, the increase in lung volume is approximately three to four times that of normal breathing. For radiotherapeutic purposes, data measured in the upright posture are relevant only in limited situations (e.g., total body irradiation with the patient standing); therefore, we include only data taken from prone, supine, and lateral positions (Peters, 1996).

2.3. Mathematics of breathing

Patients breath asymmetrically and a much-used representation, determined from x-ray fluoroscopy, is that from Lujan et al (2003), a form of which is

$$z(t) = z_0 + b \cos_{2n}(\pi t/\tau + \pi/2)$$

For motion in a z-direction where t = time, z_0 = exhale position, b = peak-to-peak amplitude, τ = breathing period and $2n$ = shape parameter. As $2n$ increases, more time is spent at end expiration. A value of 2n = 6 has often been used but extensive data fitting by George et al (2005) showed 2n = 4 modeled better but even considered cos to be adequate. If a static dose distribution is convolved with such a function it gives an approximate indication of the motion degradation. Sadly, real breathing can be more erratic with changes in amplitude, period and shape and occasional wild excursions during the breathing cycle (Seppenwoolde et al 2002, Nottrup et al 2005). This must be remembered when reading studies and motioncorrection techniques based on this equation.

2.3.1. Measuring respiratory motion

The lungs, esophagus, liver, pancreas, breast, prostate, and kidneys, among other organs, are known to move with breathing. The degradation of image quality due to this motion and subsequent effects on radiotherapy dose planning and delivery have prompted medical physicists and clinicians to study the motion using a variety of imaging modalities. The survey is not exhaustive, but is intended to provide guidelines for accommodating the motion during treatment (Vedam et al 2003).

In many cases, the object being measured is the tumor or host organ itself, while in other cases it is an artificial marker implanted in or near the tumor. In some cases, the object is a surrogate organ such as the diaphragm. Patients' breathing patterns can vary in magnitude, period, and regularity during imaging and treatment sessions, as demonstrated in Figure 2-4 (George et al 2005).

Systematic changes in the respiratory baseline also occur. Motion also varies markedly between patients, indicating that an individual approach to respiratory management is advised. Audiovisual biofeedback has been demonstrated to improve Respiratory reproducibility (Kini et al 2003).

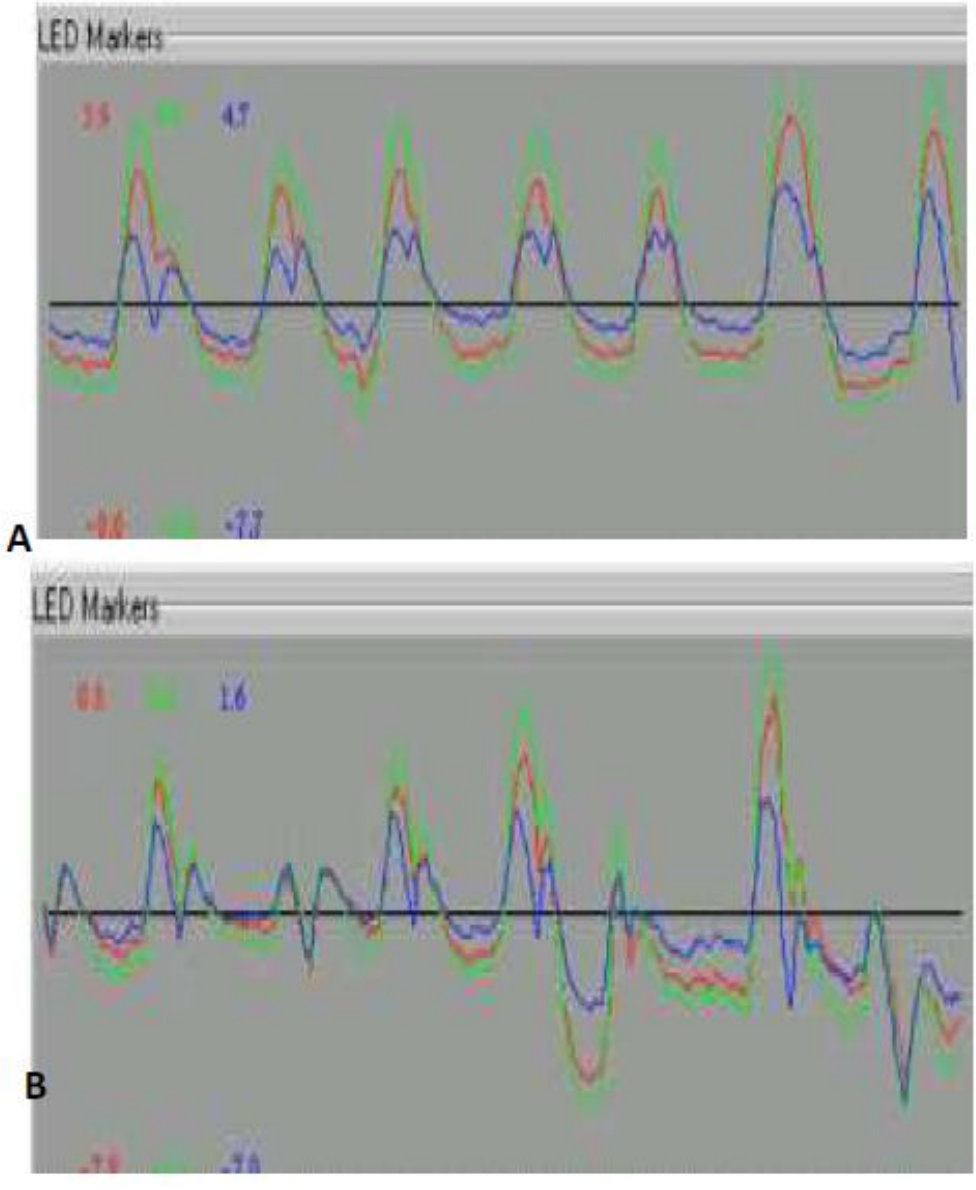

Figure 2-4. Variations in respiratory patterns form the same patient taken a few minutes apart. The three curves in each plot correspond to infrared reflected measured patient

surface in the SI, AP, and ML directions, with each component arthitraity normalized. In (a) the motion pattern is relatively reproducible in shape, displacement magnitude, and pattern. In (b) the three trace is so irregular that it is difficult to distinguish any respiratory pattern

Organ motion has been detected via ultrasound, CT (Giraud et al 2001) magnetic resonance (MR) (Korin et al 1992) , and fluoroscopy (Shimizu et al 2001), (Kubo and Hill, 2002), (Engelsman et al 2001) and Stevens et al (2001) made doubleexposure radiographs at deep inhale and deep exhale to establish the full range of lung tumor motion. Weiss et al. (1992) and Harauz and Bronskill (1999) measured liver and diaphragm motion with a gamma camera following administration of ^{99}Tc-sulphur colloid. Table 1 identifies the published observations by organ site and imaging modality.

Hanley et al, (1999), Ross et al, (1990), Grills et al (2003) and Sixel et al (2003) performed respiratory motion studies have tracked the movement of the tumor, the host organ, radiographic fiducial markers imbedded at the tumor site which studied by Ozhasoglu and Murphy (2002) and Murphy et al (2000), radioactive tracers targeting the tumor and surrogate organs, such as the diaphragm, which are assumed to correlate with the tumor. (Minohara et al 2000)

A single fluoroscopic study can provide detailed two-dimensional (2-D) information on organ motion trajectories and timing/phase shift relationships among different moving structures, but two simultaneous projections (e.g., angiography) are necessary for a complete three-dimensional (3-D) reconstruction of real-time tumor motion. These statements assume that either the anatomy or a suitable surrogate, such as an implanted fiducial marker, can be visualized. A single 2-D projection may lack the information or achieve the sufficient contrast required to recognize out-of-plane motion, rotation, or deformation of the tumor during breathing. Two CT studies acquired at inhale and exhale breath-hold may

retrospectively define the full range of tumor motion in three dimensions, but do not provide trajectory or time-profile details for the motion. This method relies on the geometric relationship between organs during breath-hold being similar to that during free breathing (FB). Vedam et al (2003) and Low et (2003) studied fourdimensional (4-D) or respiratory correlated CT using single-slice, multislice, or cone-beam acquisition can provide 3-D data on tumor position at several points along the breathing cycle with a somewhat reduced spatial resolution, as compared with conventional CT, thus providing a compromise between the good time resolution of a fluoroscopic study and the detailed 3-D information of a CT scan (Sunke et al 2003).

Multiple fiducial markers can provide a valuable indicator of tumor rotations and deformation during respiration, which is an issue that has not yet received sufficient attention in discussions of respiratory motion compensation (Taguchi, 2003).

2.3.2. Respiratory Motion observations:

Most of the published reports are based on cohorts of 10 to 30 subjects. For the tumor sites, each set of them has been condensed into a mean displacement and a full range of observed displacements. These data are summarized in (lung) and (abdomen). There are significant differences in organ motion during quiet (shallow) and deep breathing. Therefore, some of the observers have distinguished their measurements by breathing mode. Generally, abdominal organ motion is in the SI direction, with no more than a 2-mm displacement in the AP and lateral directions. However, in some individuals, the kidneys show more complex patterns.68 Lung tumor motions generally show a much greater variation in the trajectory of motion (Harauz and Bronskill, 1999).

Stevens et al. (2001) found that out of 22 lung tumor patients, 10 subjects showed no tumor motion in the SI direction. Of the remaining 12 subjects, the average SI displacement was anywhere from 3 to 22 mm (mean 8 +/– 4 mm). They found no correlation between the occurrences or magnitude of tumor motion and tumor size, location, or pulmonary function, suggesting that tumor motion should be assessed individually.

Barnes et al. (2001) found the average motion of tumors in the lower lung lobe to be significantly greater than that in the middle lobe, upper lobe, or mediastinal tumors (18.5-mm vs. 7.5-mm average SI displacement). This observation has generally been corroborated by other observations, although the individual ranges of motion are such that some individuals will show less motion in the SI direction than others will show in the AP and left–right directions.

At the time of writing, the most detailed lung tumor-motion data reported in the literature comes from the measurements of Seppenwoolde et al. (2002) who measured 3-D trajectories for 20 patients via dual real-time fluoroscopic imaging of a fiducial marker implanted in or near the tumor. They observed hysteresis in the trajectories of half the patients, amounting to a 1- to 5-mm separation of the trajectories during inhalation and exhalation, with 4 out of 20 patients exceeding a 2-mm separation. This indicates that in cases where high accuracy is required in dose alignment, a real-time tracking or gating process based on surrogate breathing signals should not only correlate with the tumor's motion along each axis with the breathing signal, but should have knowledge of the respiratory phase, because the phase difference is what leads to the hysteresis effect. In Figure 2-5, motion trajectories during radiotherapy of lung tumors, measured using implanted gold markers, are depicted. The amount of motion ranges from a 1-mm displacement to more than a 2-cm displacement. Furthermore, it can be seen that the motion is nonlinear for about half of the fiducial markers. The

majority of the fiducial markers (78% in this study) move with less than a 1cm range of motion. Similar results, based on portal imaging studies, have been reported. (Erridge et al 2003)

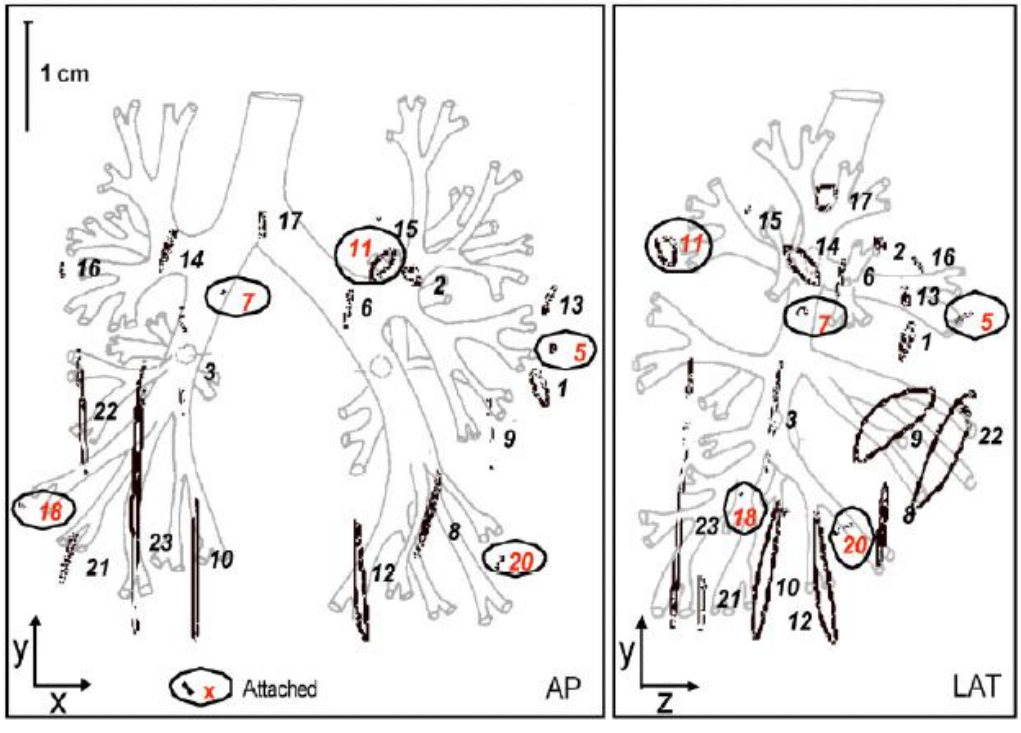

Figure 2-5. Tumor trajectories (not to scale) in 23 lung tumor patients, measured using implanted markers and real-time stereoscopic fluoroscopy. (Seppenwooldeet al 2002)

A review of the respiratory motion literature leads to the following conclusion: there are no general patterns of respiratory behavior that can be assumed for a particular patient prior to observation and treatment. The many individual characteristics of breathing quiet versus deep, chest versus abdominal, healthy versus compromised, etc. and the many motion variations associated with tumor location and pathology lead to distinct individual patterns in displacement, direction, and phase of tumor motion. Therefore, the respiratory motion pattern for each individual patient should ideally be assessed prior to treatment. Furthermore, the respiratory compensation procedures and algorithms should be adaptable to each patient's particular breathing behavior (Koch et al 2004).

In many cases, it is difficult or impossible to observe the tumor directly during treatment delivery with fluoroscopic or portal images, prompting researchers to observe surrogate internal structures, such as the diaphragm, which would be expected to have a close relationship with the tumor motion for abdominal organs and lower-lobe lung tumors, in which the mechanical coupling between tumor and diaphragm will be the strongest. However, this practice has not yet been adequately validated with data that directly correlates tumor motion with diaphragm motion, and there are known instances where it will lead to errors. For example, Iwasawa et al. (2000) reported observations of diaphragm motion in patients with emphysema. They noticed instances in which the diaphragm moved paradoxically, both as a single structure and with respect to the ventral rib cage.

Because the population of lung cancer patients presenting for radiotherapy contains many patients with compromised pulmonary function, concerns are raised about the use of the diaphragm as a surrogate indicator of lung tumor motion even in the lower lobes, where the tumor, diaphragm, and external surface motions are assumed to be the most closely coupled. Other observers notice that diaphragm motion is not necessarily related to the motion of other organs and structures in either displacement or phase. (Ford et al 2002)

If a surrogate structure, such as the chest wall or diaphragm, is used to signal tumor position for the purpose of beam gating or tracking, without observing the tumor directly during treatment, there will be uncertainties in the displacement and phase relationship between the surrogate and the tumor or other anatomy. (Ahn et al 2004) A summary of such studies is given in Table 4. It needs to be stressed that both surface markers and spirometers provide signals that are surrogates of tumor motion (Liu et al 2004).

Liu et al (2004) applications should be validated by the users performing fluoroscopic and CT imaging studies. In a gating approach to motion

compensation, the displacement correlation does not need to be known explicitly, because one is not trying to predict the absolute tumor position from the surrogate motion signal. The surrogate breathing signal only needs to indicate the phase of the breathing motion. However, it cannot be assumed a priori that the phase of the organ motion matches the phase of the surrogate motion, nor can it be assumed that the phase relationship is stationary. In fact, nonzero phase differences are evidence of either instability and nonstationary time behavior or multiple driving forces in complex oscillatory mechanical systems. These will be especially significant in the lung, where the mechanical coupling between the tumor and the surrogate structure is often weak, resulting in complex relationships between the two, and the breathing forces from the chest and/or the diaphragm. It should also be mentioned that implanted fiducial markers are also a surrogate for tumor motion, and their accuracy in depicting true tumor motion has yet to be studied (Senan et al 2001).

Ultrasound and MR real-time imaging procedures are being developed and their application to volumetrically monitor respiratory motion is appealing (Senan et al 2004).

2.4. Using MatLab Image processing in detection of tumor

MATLAB is a high-performance language for technical computing. It integrates computation, visualization, and programming in an easy-to-use environment where problems and solutions are expressed in familiar mathematical notation. Typical uses include:

- Math and computation
- Algorithm development
- Modeling, simulation, and prototyping
- Data analysis, exploration, and visualization
- Scientific and engineering graphics

- Application development, including graphical user interface building

MATLAB is an interactive system whose basic data element is an array that does not require dimensioning. This allows you to solve many technical computing problems, especially those with matrix and vector formulations, in a fraction of the time it would take to write a program in a scalar noninteractive language such as C or Fortran. Magnetic resonance imaging (MRI) has become a common way to study brain tumor. In this paper we pre-process the two-dimensional magnetic resonance images of brain and subsequently detect the tumor using edge detection technique and color based segmentation algorithm. Edge-based segmentation has been implemented using operators e.g. Sobel, Prewitt, Canny and Laplacian of Gaussian operators. The color-based segmentation method has been accomplished using K-means clustering algorithm. The color-based segmentation carefully selects the tumor from the pre-processed image as a clustering feature. The present work demonstrates that the method can successfully detect the brain tumor and thereby help the doctors for analyzing tumor size and region. The algorithms have been developed on MATLAB version 7.6.0 (R2008a) platform.

Jarritt et al (2010) stated in their study of Use of combined PET/CT images for radiotherapy planning: initial experiences in lung cancer that the potential role of positron emission tomography (PET) in radiotherapy still requires careful evaluation as it becomes increasingly integrated into the radiotherapy planning process. Diagnosis and subsequent radiotherapy planning based solely upon X-ray CT are known to be less sensitive and specific for disease than PET imaging in non-small cell lung cancer. The CT images may not demonstrate the true extent of intrathoracic disease. To overcome this limitation, the direct use of combined PET/CT image data in the treatment planning process has been investigated. A small pilot study of five patients was carried out at the Royal Victoria Hospital, Belfast, following the installation of a GE Discovery LS PET/CT scanner. The initial aims were to investigate the system and to make preliminary clinical evaluations. The key issues that were addressed included: verification of PET/CT alignment, patient position and reproducibility for imaging and treatment; verification of CT numbers on the PET/CT systems for dose calculation; integrity of data transfer; radiation protection of staff; protocols for target volume delineation; and the implications for physiologically-gated PET and CT acquisitions. This paper reviews our practical experience, and technical problems are described.

Kratochwil et al, (2010) mentioned in their study of PET/CT for diagnostics and therapy stratification of lung cancer that With the introduction of positron emission tomography (PET) and more recently the hybrid systems PET/CT, the management of cancer patients in the treatment strategy has changed tremendously. The combination of PET with multidetector CT scanning enables the integration of metabolic and high resolution morphological image information. PET/CT is nowadays an established modality for tumor detection, characterization, staging and response monitoring. The increased installation of

PET/CT systems worldwide and also the increased scientific publications underline the importance of this imaging modality. PET/CT is particular the imaging modality of choice in lung cancer staging and re-staging (T, N and M staging). The possible increased success of surgery in lung cancer patients and also the expected reduction in additional invasive diagnostics lead to benefits for both the individual patient and the healthcare system. In this review article PET and PET/CT is presented for diagnostic and therapeutic stratification in lung cancer. The fundamentals of glucose metabolism, staging, tumor recurrence and therapeutic monitoring are presented.

Jover et al (2011) stated in their study of evaluation lung cancer treatment using PET/CT scanning that PET imaging utilizes a dedicated camera system with multiple positron detector rings. PET/CT precisely aligns and combines metabolic PET mages with anatomical CT images, and is being increasingly preferred over PET scanning alone. FDG is the most widely used radiotracer in the management of cancer patients, and the prototypical PET/CT protocol used in other cancers can also be applied to the management of cervical carcinoma patients. The applications of PET/CT in cervical cancer patients include: assessing local tumor extension (information on metabolic tumor activity and possible endometrial involvement), evaluating pelvic nodal involvement (even in cases with negative CT or MRI studies), detection of distant metastases (PET/CT should be the first imaging technique used to evaluate extrapelvic disease before pelvic exenteration), radiation therapy planning (in patiens with PET scans positive for lymph nodes), identification of persistent/recurrent disease (especially in assessing response to neoadjuvant therapy and prognosis (with an inverse response-survival relationship.

Yamamoto et al, (1996) proposed a new algorithm named Quoits filter (Q-filter) to extract the isolated but low amplitude shadow located in the background which has extremely high amplitude fluctuation. Q-filter is a kind of mathematical morphology and its formulation is quite simple. This simplicity brings about a unique merit that output from this filter is analytically expressive for the case of analytical input shapes like ball, cone, or rotation of cosine function, which have characteristics of rotation symmetry and monotonic decreasing from the origin.

This Q-filter is composed of two sequential operations named Q Trans. and Q Inv.

Trans., Q Trans. corresponds to extracting feature parameters like a matched filter from the input image having a nonideal isolated shadow, and Q Inv. Trans. corresponds to restoring isolated images using extracted feature parameters. This filter is applied to detecting the cancer candidate shadow automatically in the CT cross sections of lung areas, aiming to reduce drastically the number of cross sections to be diagnosed by the doctor.

Cai, et al, (1999) carried out to present a validation study of CT and PET lung image registration and fusion based on the chamfer-matching method. Both anatomic thoracic phantom images and clinical patient images were used to evaluate the performance of our registration system. Quantitative analysis from five patients indicates that the registration error in translation was 2–3 mm in the transverse plane, 3–4 mm in the longitudinal direction, and about 1.5 degree in rotation. Typical computing time for chamfer matching is about 1 min. The total time required to register a set of CT and PET lung images, including contour extraction, was generally less than 30 min. They have implemented and validated the chamfer-matching method for CT and PET lung image registration and fusion. Our preliminary results show that the chamfer-matching method for CT

and PET images in the lung area is feasible. The described registration system has been used to facilitate target definition and treatment planning in radiotherapy.

Sudha and Jayashree (2010) conduced study to lung cancer which is among the five main types of cancer is a leading one to overall cancer mortality contributing about 1.3 million deaths/year globally. Lung cancer is a disease and it is characterized by uncontrolled cell growth in tissues of the lung. Lung nodule is an abnormality that leads to lung cancer, characterized by a small round or oval shaped growth on the lung which appears as a white shadow in the CT scan. An effective computer aided lung nodule detection system can assist radiologists in detecting lung abnormalities at an early stage. If defective nodules are detected at an early stage, the survival rate can be increased up to 50%. This paper aims to develop an efficient lung nodule detection system by performing nodule segmentation through thresholding and morphological operations. The proposed method has two stages: lung region segmentation through thresholding and then segmenting the lung nodules through thresholding and morphological operations.

Chapter Three
Materials and Methods

3.1. Materials and Methods

3.1.1. Instrumentation

- Personal Computer, with Intel Pentium IV at 1.25 MHz , 2GB RAM , 500 GB HDD , 32 x CD-DVD Drive , OS MS – Windows 9x and Printer
- Digitizer scanner
- MatLab version R2009a (7.83.2.3) program
- SPSS version 13

3.1.2. Area of Study:

This study conducted in College of Medical Radiological Science, Sudan University of Science and Technology, radiation Isotopes Center of Khartoum (RICK) in period of October 2013 to April 2014.

3.1.3. Sample Selection:

The target population amount for this study was 50 patients present at the area of the study.

3.1.4. Method of Data Collection:

In this research, to obtain more accurate results researcher divided the work into the following three stages:

1. Image Enhancement stage: To make the image better and enhance it from noising, corruption or interference.

2. Image Segmentation stage: to divide and segment the enhanced images, the used algorithms on the ROI of the image (just two lungs, the methods used are: Thresholding approach and Marker-Controlled Watershed Segmentation approach (this approach has better results than thresholding).
3. Features Extraction stage: to obtain the general features of the enhanced segmented image using Binarization and Masking Approach.

3.1.5. Method of data Analysis:

The data analyzed by using statistical package, Statistical Package for Social Studies (SPSS) under windows using t test to measure the significant difference between contrast within the soft tissues, the gray levels in both enhanced and unenhanced images and noise variance.

3.1.6. Ethical Issue:

- Permission of Radiology Department has been granted.
- No patient data will publish

Chapter Four

The results

This experimental study was conducted in College of Medical Radiological Science, Sudan University of Science and Technology, radiation Isotopes Center of Khartoum (RICK). The sample of study was included 50 patients. The main objective of this research was to study automatic data extraction in computed tomography images using morphology matching filtering.

Experimental study:

Step One: Image Enhancement stage:

To make the image better and enhance it from noising, corruption or interference. For CT images each film scanned using digitizer scanner then treated by using image processing program (MatLab), where the enhancement and contrast of the image was determined. The scanned image saved in a TIFF file format to preserve the quality of the image. The data analyzed and use to enhance the contrast within the soft tissues, the gray levels which could be redistributed both linearly and nonlinearly using the gray level frequencies and noise estimation of the original CT images. The following three methods were used for this purpose are anisotropic filtering and median filtering algorithm. The output results were compared in PSNR and MSE values. The output of filtering image applied for Image enhancement. That given image improves the subjective quality of

contrast, noise reduction and edge sharpening. The targets for image enhancing are better contrast, sharpness of detail and visibility of features. Several algorithms are Histogram Equalization (CLAHE). Here researchers applied contrast limited adaptive histogram equalization algorithm. The best PSNR value of X-ray image output is given into input of Contrast Limited Adaptive Histogram Equalization (CLAHE).

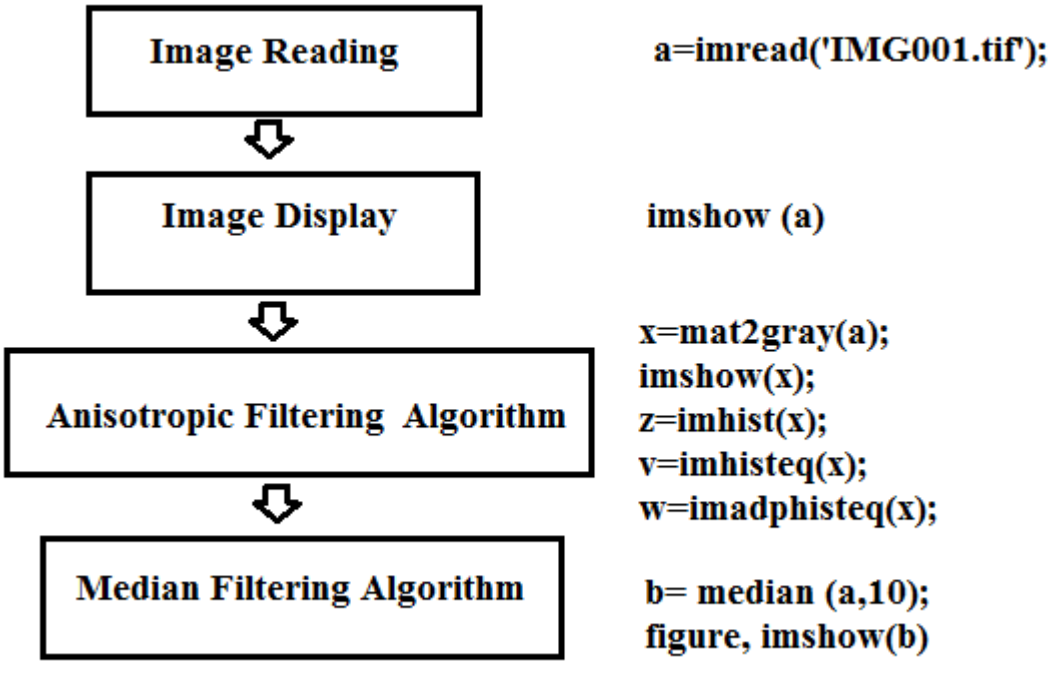

Anisotropic filtering Algorithm:

A histogram is the probability distribution of pixel values in an image. (For RGB images, the histogram is usually broken into three histograms of the three component channels.) Like any other distribution, histograms have simple

mathematical rules. Two operations that affect the pixel values, and thus the histograms, will be used extensively through these posts:

1) Adding a value to all the pixels adds that amount to the histogram; visually, this shifts the histogram.
2) Multiplying all the pixel values by a certain amount scales where the histogram data appears; visually, this stretches the histogram.

Histogram of images (imhist)

To plot the histogram of an image, there are several options. In Image Processing Toolbox, the *imhist* function is the easiest to use, but only works on single color channels. For example, to plot the green channel of an image,

```
a=imread('IMG001.tif');
x=mat2gray(a);
Z=imhist(x(:,:,2));
```

Next, the histeq function can apply the scaling:

histeq enhances the contrast of images by transforming the values in an intensity image, or the values in the colormap of an indexed image, so that the histogram of the output image approximately matches a specified histogram. *v = imhisteq(x)* transforms the intensity image I so that the histogram of the output intensity image v with length(x) bins approximately matches x. The vector x should contain integer counts for equally spaced bins with intensity values in the

appropriate range: [0, 1] for images of class double, [0, 255] for images of class uint8, and [0, 65535] for images of class uint16.

histeq automatically scales x so that *sum(x) = prod(size(I))*. The histogram of v will better match x when length(x) is much smaller than the number of discrete levels in x.

v = histeq(x,n) transforms the intensity image x, returning in v an intensity image with n discrete gray levels. A roughly equal number of pixels is mapped to each of the n levels in v, so that the histogram of v is approximately flat. (The histogram of v is flatter when n is much smaller than the number of discrete levels in x.) The default value for n is 64.

[v,T] = histeq(x,...) returns the grayscale transformation that maps gray levels in the intensity image x to gray levels in v.

v = histeq(x,map) transforms the *colormap* associated with the indexed image *X* so that the histogram of the gray component of the indexed image *(x,newmap)* approximately matches x. The *histeq* function returns the transformed *colormap* in *newmap*. length(x) must be the same as size(map,1).

newmap = histeq(x,map) transforms the values in the *colormap* so that the histogram of the gray component of the indexed image X is approximately flat. It returns the transformed *colormap* in *newmap*.

[newmap,x] = histeq(x,...) returns the grayscale transformation T that maps the gray component of map to the gray component of *newmap*. When researcher supply a desired histogram *x*, *histeq* chooses the grayscale transformation T to minimize

$$\left|c_1(T(k)) - c_0(k)\right|$$

where c_0 is the cumulative histogram of A, c_1 is the cumulative sum of x for all intensities *k*. This minimization is subject to the constraints that *T* must be monotonic and $c_1(T(a))$ cannot overshoot $c_0(a)$ by more than half the distance between the histogram counts at a. *histeq* uses this transformation to map the gray levels in x (or the *colormap*) to their new values.

$$b = T(a)$$

Median filter

The another filter median used to reduce noise in an image, somewhat like the mean filter (it is a simple, intuitive and easy to implement method of smoothing images, i.e. reducing the amount of intensity variation between one pixel and the next. It is often used to reduce noise in images). The median filter is normally used to reduce noise in an image, somewhat like the mean filter. However, it often does a better job than the mean filter of preserving useful detail in the image. Like the mean filter, the median filter considers each pixel in the image in turn and looks at its nearby neighbors to decide whether or not it is representative of its surroundings. Instead of simply replacing the pixel value with the mean of neighboring pixel values, it replaces it with the median of those values. The median is calculated by first sorting all the pixel values from the surrounding neighborhood into numerical order and then replacing the pixel being considered

with the middle pixel value. (If the neighborhood under consideration contains an even number of pixels, the average of the two middle pixel values is used.)

80	81	79	79	79	80
80	81	79	79	79	80
80	81	79	79	79	80
79	79	77	77	78	78
79	79	79	79	80	80
79	79	80	80	81	81

Figure 4-1. Sample matrix value taken from figure 4-2 (a) .

Neighborhood values: 77,77,79,79,79,79,79.79,81

Median Value is: 79

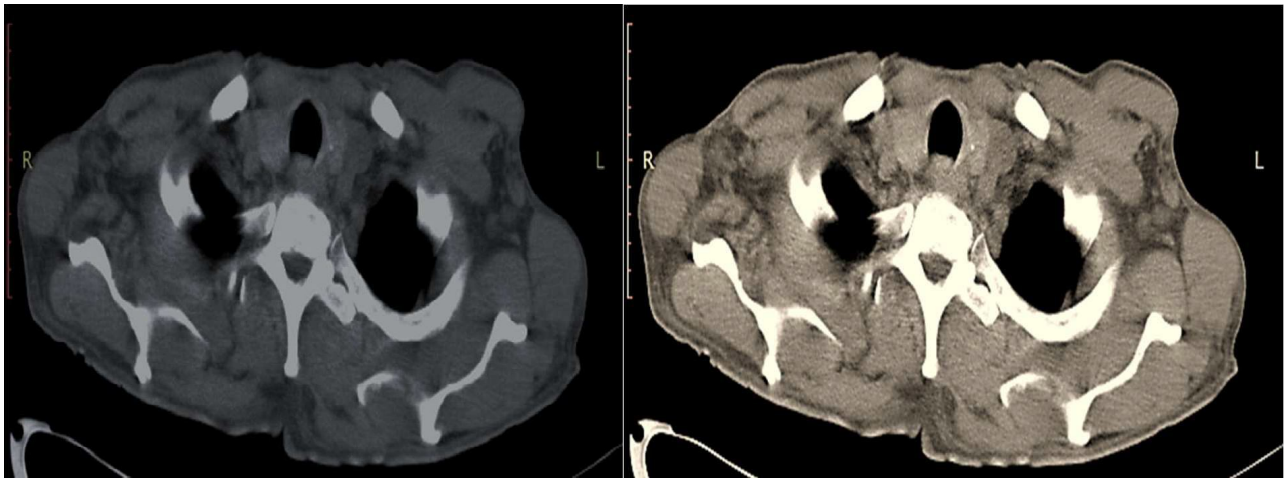

Figure 4-2. Show (a) original image used for automatic data extraction,(b) enhanced image

2. Image Segmentation stage: to divide and segment the enhanced images, the used algorithms on the ROI of the image (just two lungs, the methods used

are: Thresholding approach and Marker-Controlled Watershed Segmentation approach (this approach has better results than thresholding).

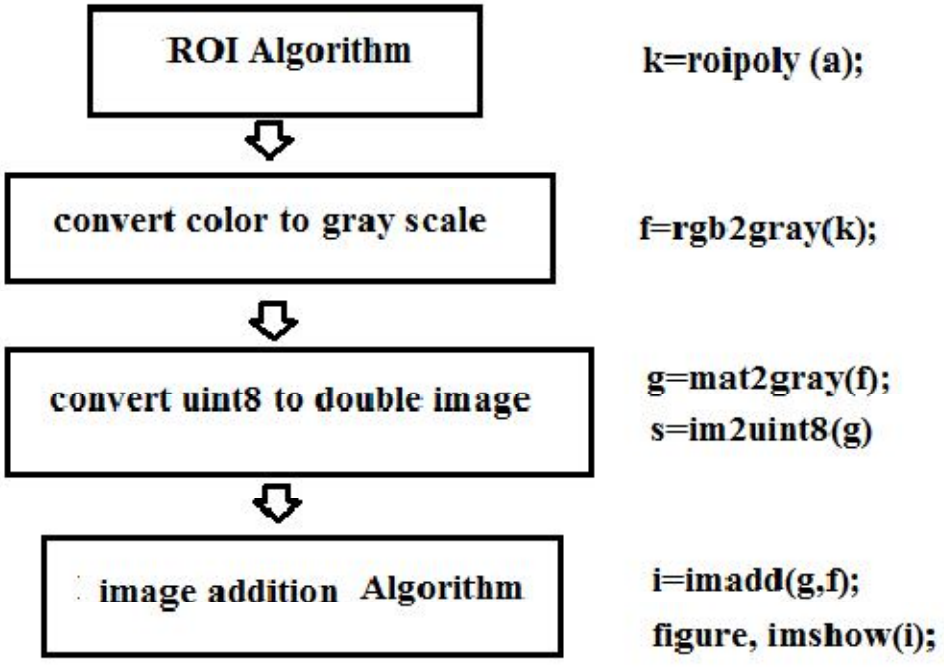

Region of Interest (ROI Algorithm):

Use *roipoly* to select a polygonal region of interest within an image. *roipoly* returns a binary image that you can use as a mask for masked filtering.

k = roipoly(a) displays the image I on the screen and lets you specify the polygon using the mouse. If researcher omit a, *roipoly* operates on the image in the current axes. Use normal button clicks to add vertices to the polygon.

Pressing *Backspace* or *Delete* removes the previously selected vertex. A shiftclick, right-click, or double-click adds a final vertex to the selection and then starts the fill; pressing *Return* finishes the selection without adding a vertex.

Image addition:

In a RGB image, the addition of two images can be done using the '+' operator.

C=A+B or imadd(g,f);

Here, the minimum value of A+B and 255 is taken.

(i.e.) *C(i,j,1)=min(A(i,j,1)+B(i,j,1),255)* where *(i,j)* represents the pixel position.

Image addition can be used to add the components from one image into other image

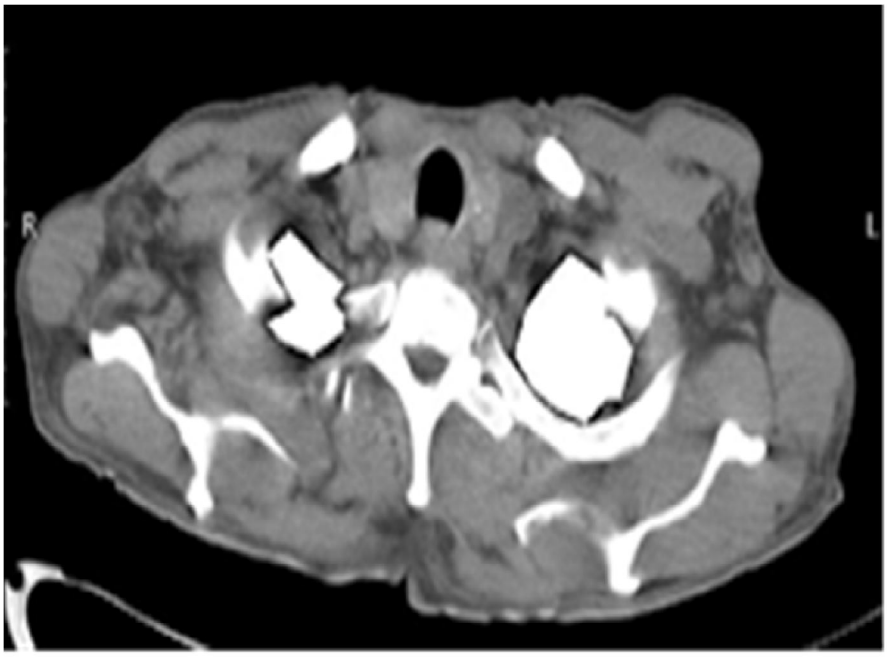

Figure 4-3. Shows image used for segmentation of lung (ROI)

3. Features Extraction stage: to obtain the general features of the enhanced segmented image using Binarization and Masking Approach (figure 4-3).

Chapter Five

Discussion, Conclusion and Recommendations

5.1. Discussion:

The results of this study and many other studies showed that lung cancer is a major cause of cancer-related deaths; it can be detected early by detecting the lung nodules. Early detection can improve the survival rate of lung cancer patients. This results supported by Sudha and Jayashree (2010) who conducted study to lung cancer which is among the five main types of cancer is a leading one to overall cancer mortality contributing about 1.3 million deaths/year globally. Lung cancer is a disease and it is characterized by uncontrolled cell growth in tissues of the lung. Lung nodule is an abnormality that leads to lung cancer, characterized by asmall round or oval shaped growth on the lung which appears as a white shadow in the CT scan. Jarritt et al, (2010), Kratochwil et al (2010) and Jover et al (2011) studied the detection of lung cancer using co-registration technique. The main ide of this project was to study automatic data extraction in computed tomography images using morphology matching filtering in order to study automatic detection of image detect lung nodule and to classify nodules as cancerous and noncancerous using Genetic Programming-based Classifier (GPC) technique. Thus the lung CT image is subjected to various processing steps and features are extracted for a set of images. Pre-processing is to improve their quality of images. If these images are too noisy or blurred they should be filtered and sharpened. In image processing, filters are mainly used to suppress either the high frequencies in the image, i.e. smoothing the images or the low frequencies, i.e. enhancing or detecting edges in the image. Due to various factors the images are in general poor in contrast. Researchers applied image pre-processing to remove artefacts and degradations such as blurring and noise. A

variety of smoothing filters have been developed that are not linear. While they cannot, in general, be submitted to Fourier analysis, their properties and domains of application have been studied extensively. For this reason researchers applied anisotropic filtering and median filtering. In study method anisotropic and median filtering algorithms were used.

The another filter median used to reduce noise in an image, somewhat like the mean filter (it is a simple, intuitive and easy to implement method of smoothing images, i.e. reducing the amount of intensity variation between one pixel and the next. It is often used to reduce noise in images). The median filter is normally used to reduce noise in an image, somewhat like the mean filter. However, it often does a better job than the mean filter of preserving useful detail in the image. Like the mean filter, the median filter considers each pixel in the image in turn and looks at its nearby neighbors to decide whether or not it is representative of its surroundings. Instead of simply replacing the pixel value with the mean of neighboring pixel values, it replaces it with the median of those values. The median is calculated by first sorting all the pixel values from the surrounding neighborhood into numerical order and then replacing the pixel being considered with the middle pixel value. (If the neighborhood under consideration contains an even number of pixels, the average of the two middle pixel values is used.). A 3×3 square neighborhood is used here larger neighborhoods produced more severe smoothing. This gray color image applied into anisotropic filtering method the output is in Figure 4-2 and also applied in median filtering algorithms the output is in Figure 4-2. Histogram equalization is a method in image processing of contrast adjustment using the image's histogram. This method usually increases the local contrast of many images, especially when the usable data of the image is represented by close contrast values. Through this adjustment, the intensities can be better distributed on the histogram. This allows for areas of lower local

contrast to gain a higher contrast without affecting the global contrast. Histogram equalization accomplishes this by effectively spreading out the most frequent intensity values. Given an image, improve the subjective quality of Contrast, Noise reduction and Edge sharpening. It operates on small pixel regions (tiles), rather than the entire image. Each tile's contrast is enhanced, so that the histogram of the output region approximately matches the specified histogram. The neighboring tiles are then combined using bilinear interpolation in order to eliminate artificially induced boundaries. The contrast, especially in homogeneous areas, can be limited in order to avoid amplifying the noise which might be present in the image. thus to see the panoramic image as a simple mixture of (unwanted) background information, diagnostic information and noise and filtered it. The detection of the noise is a complex procedure which is difficult to detect by naked eye so that image analysis should be performed by using powerful image processing. The processing steps include thresholding, morphological operations and feature extraction. By using these steps the nodules are detected and segmented and some features are extracted. The extracted features are tabulated for future classification.

5.2. Conclusion:

A variety of smoothing filters have been developed that are not linear. While they cannot, in general, be submitted to Fourier analysis, their properties and domains of application have been studied extensively. So conclusion of this research that the new approach is funded on an attempt to interpret the problem from the view of blind source separation (BSS). The extracted features are tabulated for future classification.

5.3. Recommendations:

- The study proposed a new approach of lung tissue extraction using image processing technique (MATLAB) with limited applications and I hope from the other researchers to continue on other applications and toolbox.
- Image pre-processing techniques can easily remove artefacts and degradations such as blurring and noise so I recommended other researcher to use those techniques.
- The future work of this project is to identify the effective features for further classification. Genetic Programming-based Classifier will be used for classification of lung CT images as cancerous and non-cancerous by using the identified effective features.

References:

1. Clemente CD. 1997, Anatomy: A regional atlas of the human body. 3rd ed. Baltimore, MD: Urban & Schwartzenberg.

2. Collins JD, Shaver ML, Batra P. Brown K. Nerves on magnetic resonance imaging. J Natl Med Assoc. 1989;81 (2):129-134.

3. Collins JD, Shaver ML, Batra P, Brown K. Anatomy of the upper and lower extremity muscle and tendon insertions as displayed by magnetic resonance imaging. Anat Rec.1 988;224(4):24A.

4. Collins JD, Batra P, Brown RK, Winter J, King W. Computerized chest tomography in asbestos workers suspected of having pleural disease. J Natl Med Assoc. 1 987;79(3):273-277.

5. Cameron L, Ord VA, Fullerton GD. Characterization of proton NMR relaxation times in normal and pathological tissues by correlation with other tissue parameters. Magn Reson Imaging. 1984;2:97-106.

6. Collins JD, Shaver ML, Kovacs BJ, et al. Enhancing magnetic resonance images using water bags. J Natl Med Assoc. 1990;3:197-200.

7. Masih S, Bakhda RK, Collins JD. Pelvic fused kidneys: Magnetic resonance imaging and intravenous pyelogram correlation. J Natl Med Assoc. 1988;(8):925-927.

8. Abdelnour, A.F., Nehmeh, S.A., Pan, T., Humm, J.L., Vernon, P., Schoder, H., Rosenzweig, K.E., Mageras, G.S., Yorke, E., Larson, S.M., Erdi, Y.E. (2003), Phase and amplitude binning for 4D-CT imaging, Journal of Medical Physics and Biology,vol.52, P.p.3515-3529.

9. Ahn, S., B. Yi, Y. Suh, J. Kim, S. Lee, S. Shin, S. Shin, and E. Choi. (2004). "A feasibility study on the prediction of tumour location in the lung from skin motion, British Journal of Radiology, Vol.77(919):P.p.588–596.

10.Alheit H, Dornfeld S, Winkler C, Blank H and Geyer P,2000, Stereotactic guided irradiation in prostatic cancer using the ExacTrac-System (BrainLab), Journal of Radiotherapy and Oncology, Vol.56 (Suppl. 1):P.p.107

11.Allen AM, Siracuse KM, Hayman J A and Balter JM, 2004,Evaluation of the influence of breathing on the movement and modeling of lung tumors,International Journal of Radiation Oncology and Biology Physics, Vol.58:P.p.1251–7

12.Arnold, V.I, 1997, Mathematical Methods of Classical Mechanics, 2nd edn, Springer, England.

13.Artignan X, Smitsmans M H P, de Bois J, Lebesque J V, van Herk M and Bartelink, 2002, On-line ultrasoundimage guidance for radiotherapy of prostate cancer: the impact of image acquisition on prostate displacement, Journal of Radiotherapy and Oncology, Vol.64 (Suppl. 1):P.p.279

14.Artignan X, Smitsmans M H P, Lebesque J V, Jaffray D A, van Herk M and Bartelink, 2004, Online ultrasound image guidance for radiotherapy of prostate cancer: impact of image acquisition on prostate displacement, International Journal of Radiation Oncology and Biology Physics, Vol.59:P.p.595–601

15.Aubrey J-F, Beaulieu L, Girouard L-M, Aubin S, Tremblay D, Laverdiere J and Vigneault,2004, Measurements of intrafraction motion and interfraction and intrafraction rotation of prostate by three-dimensional analysis of daily portal imaging with radiopaque markers,International Journal of Radiation Oncology and Biology Physics, Vol.60,P.p.30–9

16.Aznar M C, Sixel K E and Ung Y C, 2000 Feasibility of deep inspiration breath hold combined with intensity modulated radiation treatment delivery for left sided breast cancer Proc., 42th Annual ASTRO Meeting, International Journal of Radiation Oncology and Biology Physics, Vol.48 (Suppl.)P.p.297

17.Balter J M, Litzenberg D W, Brock K K, Sanda M, Sullivan M, Sandler H M and Dawson L A, 2000, Ventilatory movement of the prostate during radiotherapy. Proc., 42th Annual ASTRO Meeting, International Journal of Radiation Oncology and Biology Physics, Vol.48 (Suppl.)P.p.167

18.Balter J M, Wright J N, Newell L J, Friemel B, Dimmer S, Cheng Y, Wong J, Vertatschitsch E and Mate T P, 2005, Accuracy of a wireless localization system. for radiotherapy,International Journal of Radiation Oncology and Biology Physics, Vol.61, P.p.933–937

19.Balter J, Wright N, Dimmer S, Friemel B, Newell J, Cheng Y andMate T,2003,Demonstration of accurate localisation and continuous tracking of implantable wires, International Journal of Radiation Oncology and Biology Physics, Vol.57, P.p.264

20.Balter, J. M., K. L. Lam, C. J. McGinn, T. S. Lawrence, and R. K. Ten Haken, 1998, Improvement of CT-based treatment-planning models of abdominal targets using static exhale imaging, International Journal of Radiation Oncology and Biology Physics,vol.41(4):P.p.939–943.

21.Barnes E A, Murray B R, Robinson D M, Underwood L J, Hanson J and Roa W H Y,2001,Dosimetric evaluation of lung tumour immobilization using breath hold at deep inspiration, International Journal of Radiation Oncology and Biology Physics, Vol.50, P.p.1091–1098

22.Barnes, E. A., B. R. Murray, D. M. Robinson, L. J. Underwood, J. Hanson, and W. H. Roa, 2001, Dosimetric evaluation of lung tumor immobilization using breath hold at deep inspiration,International Journal of Radiation Oncology and Biology Physics,vol.50(4):P.p.1091–1098.

23.Beckham, W. A., P. J. Keall, and J. V. Siebers, 2002, A fluence-convolution method to calculate radiation therapy dose distributions that incorporate random set-up error, Journal of Medical Physics and Biology, vol.47 (19):P.p.3465–3473.
24.Beg, M.F., Miller, M.I., Trouv e, A., Younes, L.: Computing large deformation metric mappings via geodesic ows of di eomorphisms. International Journal of Computer and Visualization, Vol.61-P.p.139-157
25.Berbeco R I, Mostafavi H, Sharp G C and Jiang S B 2005a Towards fluoroscopic respiratory gating for lung tumours without radiopaque markers,Journal of Medical Physics and Biology,vol.50, P.p.4481–4490
26.Berbeco R I, Neicu T, Rietzel E, Chen G T Y and Jiang S B, 2005, A technique for respiratory-gated radiotherapy treatment verification with an EPID in cine mode, Journal of Medical Physics and Biology,vol.50P.p.3669–3679
27.Berbeco R I, Nishioka S, Shirato H, Chen G T Y and Jiang S B, 2005, Residual motion of lung tumours in gated radiotherapy with external respiratory surrogates, Journal of Medical Physics and Biology, vol. 50P.p.3655–3667
28.Berbeco, R. I., S. Nishioka, H. Shirato, G. T. Chen, and S. B. Jiang, 2005, Residual motion of lung tumors in gated radiotherapy with external respiratory surrogates, Journal of Medical Physics and Biology,vol.50(16):P.p.3655–3667

29.Berbeco, R. I., S. Nishioka, H. Shirato, G. T. Chen, and S. B. Jiang, 2005, Residual motion of lung tumours in gated radiotherapy with external respiratory surrogates, Journal of Medical Physics and Biology, vol.50(16): P.p.3655–3667.

30.Berbeco, R. I., T. Neicu, E. Rietzel, G. T. Chen, and S. B. Jiang, 2005, A technique for respiratory gated radiotherapy treatment verification with an EPID in cine mode, Journal of Medical Physics and Biology, vol.50 (16):P.p.3669–3679.

31.Berson, A. M., R. Emery, L. Rodriguez, G. M. Richards, T. Ng, S. Sanghavi, and J. Barsa. (2004). “Clinical experience using respiratory gated radiation therapy: Comparison of free breathing and breath-hold techniques, International Journal of Radiation Oncology and Biology Physics, Vol.60 (2): P.p.419–426.

32.Bosmans, G., van Baardwijk, A., Dekker, A., Ollers, M., Boersma, L., Minken, A., Lambin, P., Ruysscher, D.D., 2006, Intra-patient variability of tumor volume and tumor motion during conventionally fractionated radiotherapy for locally advanced non-small- cell lung cancer: A prospective clinical study, International Journal of Radiation Oncology and Biology Physics, Vol.66,P.p.748- 753

33.Bowden, P., R. Fisher, M. Mac Manus, A. Wirth, G. Duchesne, M. Millward, A. McKenzie, J. Andrews, and D. Ball, 2002, Measurement of lung tumor volumes using three-dimensional computer planning software, International Journal of Radiation Oncology and Biology Physics, vol.53(3): P.p.566–573.

34.Cantarella, J., DeTurck, D., Gluck, H.: Vector calculus and the topology of domains in 3-space. American Journal of Mathematic Vol.109,P.p.409-442

35.Chen, Q. S., M. S. Weinhous, F. C. Deibel, J. P. Ciezki, and R. M. Macklis., 2005, “Fluoroscopic study of tumor motion due to breathing: Facilitating precise radiation therapy for lung cancer patients, Journal of Medical Physics and Biology, vol.28 (9): P.p.1850–1856.

36.Davies, S. C., A. L. Hill, R. B. Holmes, M. Halliwell, and P. C. Jackson, 1994, Ultrasound quantitation of respiratory organ motion in the upper abdomen, British Journal of Radiology, Vol.67 (803):P.p.1096–1102.

37.De Koste, J. R., F. J. Lagerwaard, H. C. de Boer, M. R. Nijssen-Visser, and S. Senan, 2003, Are multiple CT scans required for planning curative radiotherapy in lung tumors of the lower lobe?, International Journal of Radiation Oncology and Biology Physics, vol.55 (5): P.p.1394–1399.

38.Ehrhardt, J., Werner, R., Siaring, D., Frenzel, T., Lu, W., Low, D., Handels, H.: An optical how based method for improved reconstruction of 4D CT data sets acquired during free breathing, Journal of Medical Physics and Biology, vol.34, P.p.711-721

39.Engelsman, M., E. M. Damen, K. De Jaeger, K. M. van Ingen, and B. J. Mijnheer, 2001, The effect of breathing and set-up errors on the cumulative dose to a lung tumor, Radiotherapy Oncology, vol.60 (1): P.p.95–105

40.Erridge, S. C., Y. Seppenwoolde, S. H. Muller, M. van Herk, K. De Jaeger, J. S. Belderbos, L. J. Boersma, and J. V. Lebesque, 2003, Portal imaging to assess setup errors, tumor motion and tumor shrinkage during conformal radiotherapy of non-small cell lung cancer, Journal of Radiotherapy and Oncology, Vol.66 (1): P.p.75–85.

41.Essapen, S., C. Knowles, A. Norman, and D. Tait, 2002, Accuracy of set-up of thoracic radiotherapy: prospective analysis of 24 patients treated with radiotherapy for lung cancer, British Journel Radiology, vol.75 (890): P.p.162 169.

42.Essapen, S., C. Knowles, and D. Tait,2001, Variation in size and position of the planning target volume in the transverse plane owing to respiratory movement during radiotherapy to the lung, British Journal of Radiology, Vol.74 (877): P.p.73–76.

43.Ford, E. C., G. S. Mageras, E. Yorke, and C. C. Ling, 2003, Respirationcorrelated spiral CT: A method of measuring respiratory-induced anatomic motion for radiation treatment planning, Journal of Medical Physics and Biology, vol.30(1): P.p.88–97.

44.Fowler, J. F., W. A. Tome, J. D. Fenwick, and M. P. Mehta, 2004, A challenge to traditional radiation oncology, International Journal of Radiation Oncology and Biology Physics, vol.60(4): P.p.1241–1256

45.George, R., S. S. Vedam, T. D. Chung, V. Ramakrishnan, and P. J. Keall, 2005, The application of the sinusoidal model to lung cancer patient respiratory motion,Journal of Medical Physics and Biology, vol.32(9): P.p.2850–2861.

46.Giraud, P., M. Antoine, A. Larrouy, B. Milleron, P. Callard, Y. De Rycke, M. F. Carette, J. C. Rosenwald, J. M. Cosset, M. Housset, and E. Touboul, 2000, Evaluation of microscopic tumor extension in non-small-cell lung cancer for threedimensional conformal radiotherapy planning, International Journal of Radiation Oncology and Biology Physics, vol.48(4): P.p.1015–1024.

47.Giraud, P., Y. De Rycke, B. Dubray, S. Helfre, D. Voican, L. Guo, J. C. Rosenwald, K. Keraudy, M. Housset, E. Touboul, and J. M. Cosset., 2001, "Conformal radiotherapy (CRT) planning for lung cancer: analysis of intrathoracic organ motion during extreme phases of breathing,International Journal of Radiation Oncology and Biology Physics, vol.51(4): P.p.1081–1092.

48.Grills, I. S., D. Yan, A. A. Martinez, F. A. Vicini, J. W. Wong, and L. L. Kestin, 2003, Potential for reduced toxicity and dose escalation in the treatment of inoperable non-small-cell lung cancer: A comparison of intensity-modulated radiation therapy (IMRT), 3D conformal radiation, and elective nodal irradiation, International Journal of Radiation Oncology and Biology Physics, vol.57(3): P.p.875–890.

49.H. U. Lemke, M. W. Vannier, K. Inamura, A. G. Farman, and K. Doi, 2002, Proceedings of the 16th International Congress on Computer-Assisted Radiology and Surgery (CARS), June 2002 Paris, France. Heidelberg: Springer-Verlag, P.p.539–544.

50.Hanley, J., M. M. Debois, D. Mah, G. S. Mageras, A. Raben, K. Rosenzweig, B. Mychalczak, L. H. Schwartz, P. J. Gloeggler, W. Lutz, C. C. Ling, S. A. Leibel,

Z. Fuks, and G. J. Kutcher, 1999, Deep inspiration breath-hold technique for lung tumors: The potential value of target immobilization and reduced lung density in dose escalation, International Journal of Radiation Oncology and Biology Physics, vol.45(3): P.p.603–611.

51.Hara, R., J. Itami, T. Kondo, T. Aruga, Y. Abe, M. Ito, M. Fuse, D. Shinohara, T. Nagaoka, and T. Kobiki, 2002, Stereotactic single high dose irradiation of lung tumors under respiratory gating, Journal of Radiotherapy and Oncology, Vol.63(2): P.p.159–163.